SUPPLEMENTARY INFORMATION

Supplementary Tables

Supplementary Table S1. Supporting data for callus cell atlas and chemical screen.

Sheet 1. Statistical summary of scRNA-seq data.

Sheet 2. Top cluster marker genes at CIM0.

Sheet 3. Top cluster marker genes at CIM1.

Sheet 4. Top cluster marker genes at CIM3.

Sheet 5. Top cluster marker genes at CIM7.

Sheet 6. Protoplasting responsive genes.

Sheet 7. Abbreviations and IDs of differentially expressed genes.

Sheet 8. Binary constructs used for cell cluster annotation in this study.

Sheet 9. Primers used in this study.

Sheet 10. Gene list for *in situ* RNA sequencing.

Sheet 11. Chemical library used in this study.

Sheet 12. Representative GO terms enriched among differentially expressed genes under U0126 treatment at CIM7.

Sheet 13. Representative PO terms enriched among differentially expressed genes under U0126 treatment at CIM7.

Sheet 14. Representative GO terms enriched among differentially expressed genes under U0126 treatment at SIM6.

Sheet 15. Representative PO terms enriched among differentially expressed genes under U0126 treatment at SIM6.

Sheet 16. Representative GO terms enriched among differentially expressed genes under ES treatment in *mkk4,5RNAi-est* calli at CIM7.

Sheet 17. Representative PO terms enriched among differentially expressed genes under ES treatment in *mkk4,5RNAi-est* calli at CIM7.

Sheet 18. Other MEK inhibitors from TargetMol.

Sheet 19. Differential CUT&Tag-seq peaks between $PLT1^+$ and $YUC3^+$ cells.

Sheet 20. Differential CUT&Tag-seq peaks between $PLT1^+$ and $ACL5^+$ cells.

Sheet 21. Differential ATAC-seq peaks between $PLT1^+$ and $YUC3^+$ cells.

Sheet 22. Differential ATAC-seq peaks between $PLT1^+$ and $ACL5^+$ cells.

Sheet 23. Mass-spectrometry-based phosphoproteomic analysis results.

Sheet 24. Representative enriched GO terms for downregulated phosphopeptides in the U0126-treated sample.

Supplementary Videos

Supplementary Video S1. Tracking cell division patterns of ACRs and FCRs using live imaging with PlaCCI.

Distinct fluorescence signals were used to distinguish G1 (Cyan), S (Red), and G2–M (Yellow) cell cycle phases. A total of 66 time-lapse rounds (T1–T66) were acquired at 40-min intervals. The elapsed time (in hours, h) is shown at the top left corner. Scale bars, 50 μm.

Supplementary Video S2. Tracking cell division patterns of a mock callus using live imaging with PlaCCI.

Distinct fluorescence signals were used to distinguish G1 (Cyan), S (Red), and G2–M (Yellow) cell cycle phases. A total of 66 time-lapse rounds (T1–T66) were acquired at 40-min intervals. The elapsed time (in hours, h) is shown at the top left corner. Scale bars, 50 μm.

Supplementary Video S3. Tracking cell division patterns of a U0126-treated callus using live imaging with PlaCCI.

Distinct fluorescence signals were used to distinguish G1 (Cyan), S (Red), and G2–M (Yellow) cell cycle phases. A total of 66 time-lapse rounds (T1–T66) were acquired at 40-min intervals. The elapsed time (in hours, h) is displayed at the top left corner. Non-nuclear cyan signals observed in the epidermal and cortex cells of U0126-treated samples were due to U0126 autofluorescence. Scale bars, 50 μm.

Text S1

Annotation of the cell atlas

For scRNA-seq, two biological replicates were performed for each time point except CIM7 (Supplementary Fig. S1a). After quality control and filtering, the dataset included 101,261 single-cell transcriptomes: 23,174 from CIM0, 31,283 from CIM1, 33,583 from CIM3, and 13,221 from CIM7 (Supplementary Table S1).

To mitigate transcriptomic artifacts induced by protoplasting, we conducted bulk RNA sequencing (RNA-seq) of both protoplasts and intact calli at each time point, identifying differentially upregulated protoplasting-induced genes (Supplementary Table S1). By intersecting gene sets across all four time points, we identified 284 protoplasting-induced genes (Supplementary Fig. S1b; Supplementary Table S1). We excluded these genes to avoid the influence of protoplast preparation on clustering, annotation, and integration of single cells and subsequent selection of highly variable genes for single-cell analysis. The quality of single-cell transcriptomes was validated by pseudo-bulking transcriptomes for each library. Principal component analysis (PCA) demonstrated a strong correlation between pseudo-bulk transcriptomes and bulk RNA-seq at corresponding time points (Supplementary Fig. S1a) [1], confirming that scRNA-seq accurately captured representative callus cell populations.

At CIM0, clusters 2 and 9 were adjacent on the UMAP plot, representing the epidermis and cortex, respectively (Fig. 1a). Epidermis markers included *JACALIN-RELATED LECTIN 31* (*JAL31, AT3G16430*), *JAL22* (*AT2G39310*), and *3-KETOACYL-COA SYNTHASE 10* (*KCS10*, *AT2G26250*) [2]. The cortex-specific gene *IQM1* (*AT4G33050*) [3], and shared epidermis/cortex markers *PUP7* (*AT4G18197*) and *MLP329* (*AT2G01530*) further supported these annotations (Supplementary Fig. S1c, d). Cluster 8 was assigned to companion cells based on *AT1G54575* expression (Supplementary Fig. S1c, d).

Cluster 3 was identified as pericycle cells using *USUALLY MULTIPLE ACIDS MOVE IN AND OUT TRANSPORTERS 18* (*UMAMIT18*, *AT1G44800*) (Fig. 1a; Supplementary Fig. S1c, d). Clusters 1,4, 5, and 13 corresponded to procambium, supported by *PHLOEM PROTEIN 2-B14* (*PP2-B14*,

AT1G56250), *ABNORMAL SHOOT 5* (*ABS5*, *AT1G68810*), and *ACAULIS 5* (*ACL5*, *AT5G19530*) expression (Fig. 1a; Supplementary Fig. S1c, d) [4-6]. Additional markers such as *AT2G21560*, *AT5G19875*, *AtbZIP7* (*AT4G37730*), *RHA2B* (*AT2G01150*), and *PEPTIDE 1* (*PEP1*, *AT5G64900*) were expressed in both pericycle and procambium.

Cluster 10 represented phloem sieve elements (SE) and xylem tracheary elements (TE) (Fig. 1a). While *AT1G08160* was exclusively expressed in SE, *GERMIN-LIKE PROTEIN 10* (*GLP10*, *AT3G62020*) was only active in TE (Supplementary Fig. S1c, d). Cluster 11 likely corresponded to guard cells on the hypocotyl epidermis, validated by *TRYPSIN INHIBITOR PROTEIN 2* (*ATTI2*, *AT2G43520*) expression (Fig. 1a; Supplementary Fig. S1c, d).

Finally, several wound-responsive genes, including *WOUND INDUCED DEDIFFERENTIATION 1* (*WIND1*, *AT1G78080*) and *WIND2* (*AT1G22190*), were highly expressed in clusters 6, 7, and 12 (Fig. 1a; Supplementary Fig. S1c, d) [7-10]. The pericycle and procambium-marker genes *AT5G19875*, *AtbZIP7*, *RHA2B*, and *PEP1* were detected within these three clusters (Supplementary Fig. S1c, d). We therefore annotated them as wound-responsive pericycle and procambium cells. We did not capture a sufficient number of endodermis cells at CIM0, likely due to unidentified cell wall modifications hindering efficient protoplasting.

At CIM1, the cell atlas separated into three major territories: epidermis/cortex, pericycle/callus cells, and procambium (Fig. 1b; Supplementary Fig. S2a, c). Procambium clusters resembled those at CIM0 (Fig. 1a), while the pericycle territory divided into three clusters (3, 10, and 12) (Fig. 1b). Cluster 3 likely represented quiescent pericycle cells, whereas clusters 10 and 12 reflected proliferating pericycle cells forming callus (Fig. 1b). Wound-responsive clusters (6, 13, and 2) were also identified within the epidermis, cortex, and procambium territories (Fig. 1b; Supplementary Fig. S2b, c).

At CIM3, the primary territories corresponding to the epidermis/cortex and procambium remained largely consistent (Fig. 1c; Supplementary Fig. S3a–c, h). However, callus cell clusters (clusters 4 and 6), derived from the pericycle territory, became more prominent (Supplementary Fig. S3d–f). Supporting the idea that *A. thaliana* callus formation follows a root developmental pathway, these

clusters showed high enrichment for root identity genes, including *WOX5* and *PLT1* (Supplementary Fig. S3e) [11,12]. Additionally, clusters corresponding to endodermis (cluster 13), TE (cluster 15), and phloem companion cells (cluster 8) were identified (Supplementary Fig. S3a, g). At CIM7, the proportion of callus cells increased further (Fig. 1d). Consistent with previous studies [11,13], we identified three distinct callus layers: outer (clusters 3 and 4), middle (cluster 8), and inner (clusters 2 and 9) (Fig. 1d; Supplementary Fig. S3i and S4).

To gain a comprehensive understanding, we performed an integrated analysis of single-cell transcriptome data from all four time points (Fig. 1e). The most pronounced transcriptomic changes occurred from CIM0 to CIM1, aligning with our earlier findings [1]. Collectively, this time-resolved scRNA-seq analysis generated a detailed cell atlas for *A. thaliana* callus, capturing the dynamic changes in cell types throughout callus development.

We then employed IISS to validate and refine the above annotations (see Methods). Based on our cell atlas annotations (Supplementary Table S1), we designed RNA probes for over 100 representative genes and generated a spatial transcriptomic map for the CIM7 callus. Through this spatial analysis, we identified five novel cell types (N1 to N5) that could not be spatially resolved via scRNA-seq (Fig. 2b, c; see Main text for details).

Briefly, N1 and N2 cells were localized to FCR and ACR, respectively (Supplementary Fig. S5a). *LACS2*, *GGL12*, and *CYP77B1* were preferentially expressed in the FCR, whereas *KCS16* was principally restricted to the ACR (Supplementary Fig. S4b and S5b–d). Other marker genes for N2 included *IAA7* and *ABCB15* (Supplementary Fig. S5e-g).

N3 cells were located in the L2–L5 layers of the ACR and marked by genes such as *YUC3*, *YUC8*, and *CYP79B2* (Supplementary Fig. S4b, S6a, b). Several root cap genes, including *BRN1*, *BRN2*, and *SMB* were specifically expressed in N2 (Supplementary Fig. S6c, d).

N4 cells were identified using *AT2G22510* and *PELPK1* as markers (Supplementary Fig. S4b and S6e–g). Notably, these cells were enriched in genes associated with cell death and senescence, including *BFN1*, *SAG29*, *RNS3*, *MC9*, *EXI1*, and *DMP4* (Supplementary Fig. S6h). Given their similarities to the cells in the SIM6 cell atlas by Ogura et al. (Supplementary Fig. S6h) [13], we

concluded that N4 cells represent "fully differentiated callus cells" that have lost their pluripotency (Fig. 2c).

N5 cells were predominantly located in the inner ACR and vascular tissues of explants. The markers genes included *ABS5*, *SMXL3*, *XYP2*, *HB8*, and *ACL5* (Supplementary Fig. S7a–c). Notably, *ACL5* and *ABS5*-positive cells exhibited a striped pattern resembling vascular organization (Supplementary Fig. S7b, c).

Tracking of the cell fate of FCRs

The FCRs have fewer cell layers compared to the ACRs. This observation raises the question of whether FCRs represent an early developmental state of ACRs. To investigate this, we conducted a long-term tracking of cell fate in FCRs. As shown in Supplementary Fig. 10d and e, around 44% of FCRs maintained their original state at CIM14, while 36% of FCRs ultimately disappeared due to compression from the surrounding two ACRs. Interestingly, approximately 20% of FCRs developed into ACRs. These results suggest that our assessment of FCRs at CIM7 may not have been entirely accurate. The asynchronous development of ACRs might lead to some ACRs at early developmental stages being misclassified as FCRs. Nevertheless, since nearly half of the FCRs still retain their original state, these findings imply that FCRs are likely not an early developmental state of ACRs.

Epigenetic profiling of ACRs and FCRs

Epigenetic regulation plays a central role in governing cell fate transitions during callus induction and shoot formation [1,14,15]. To elucidate why ACRs lose their shoot regeneration competence, we compared the epigenetic landscapes of ACRs and FCRs. Because direct microdissection-based profiling of ACRs and FCRs is technically challenging, we developed fluorescence-activated cell sorting (FACS)-based CUT&Tag and ATAC-seq approaches optimized for trace amounts of plant tissue (see Methods) [16-18].

However, a dedicated reporter for FCRs is currently unavailable. As previously noted, *PLT1* is expressed in both ACRs and FCRs, whereas *YUC3* and *ACL5* are specifically expressed in ACRs (Supplementary Fig. S4a and S11b). Therefore, we used PLT1-positive ($PLT1^+$) cells to represent both ACRs and FCRs, while $ACL5^+$ and $YUC3^+$ cells served as ACR-specific populations. The sorted cells

were subjected to CUT&Tag profiling for the repressive histone mark H3K27me3 (Supplementary Fig. S11c–e) and to ATAC-seq to assess chromatin accessibility (Supplementary Fig. S11h–j). Comparisons between PLT1$^+$ and ACL5$^+$/YUC3$^+$ cells provided an approximate evaluation of epigenetic differences between ACRs and FCRs.

As shown in Supplementary Fig. S11f, g, no significant differences were detected in H3K27me3 enrichment at loci associated with shoot regeneration among PLT1$^+$, ACL5$^+$, and YUC3$^+$ cells. In contrast, consistent with previous findings that cell fate transitions during shoot regeneration depend on chromatin accessibility dynamics [1], loci of key shoot-related genes such as *WUS*, *STM*, *YABBY5* (*YAB5*), and *ENHANCER OF SHOOT REGENERATION1* (*ESR1*) remained largely inaccessible in ACL5$^+$ and YUC3$^+$ cells (Supplementary Fig. S11k–n). Notably, genes conferring root cap and vascular identities, including *FEZ*, *CYP79B2*, *ABS5*, and *VASCULAR-RELATED NAC-DOMAIN7* (*VND7*), exhibited increased accessibility in the corresponding cells (Supplementary Fig. S11l, n). Shoot-associated genes exhibited a combination of repressive histone modifications and increased chromatin accessibility within FCRs, indicating a poised regulatory state in which H3K27me3 likely functions as a silencing constraint. Consistent with this model, recent work has shown that distal regulatory elements linked to developmental genes display hallmark features of poised enhancers, including high accessibility together with elevated H3K27me3 levels [19].

Taken together, cell fate tracing and epigenetic profiling results indicate that most ACRs have adopted a root-like identity while simultaneously losing the open chromatin configuration required for shoot regeneration.

Phosphoproteomic analysis of the mechanisms of action of U0126

To further elucidate the molecular mechanisms by which U0126 reduces ineffective callus regions via the MKK4/5–MPK3/6 pathway, we performed mass spectrometry–based phosphoproteomic analysis on mock- and U0126-treated calli. Across five biological replicates, a total of 53,312 phosphopeptides derived from 12,626 proteins were identified (Supplementary Fig. S17a, b and Table S1). In agreement with previous findings [20], phosphorylation of MPK6 at T221 and Y223—sites targeted by MKK4/5—was reduced in U0126-treated samples (Supplementary Fig. S17c). Moreover,

hypophosphorylated peptides in U0126-treated calli were enriched for proline-directed SP motifs, a canonical recognition site for MAPK (Supplementary Fig. S17d and Table S1) [21-24]. Differential phosphoproteomic analysis further revealed substantial decreases in the phosphorylation of proteins implicated in epigenetic regulation, the cell cycle, and auxin transport following U0126 treatment (Supplementary Fig. S17e).

Limitation of U0126

We also evaluated U0126 in *Brassica napus* variety Westar (spring-type). Unlike ZS11 and Tapidor, U0126 did significantly enhanced shoot regeneration in Westar (Supplementary Fig. S18c, d). Investigations into Westar's callus morphology revealed limited callus formation at the wound site and weak cell proliferation in the middle hypocotyl (Supplementary Fig. S18d). We hypothesized that reduced hormone permeability in Westar hypocotyls might impede auxin uptake, limiting callus development and rendering U0126 ineffective.

To test this, we applied permeability-enhancing treatments: (1) a squeeze treatment to mechanically disrupt tissue, and (2) n-hexane soaking to overcome potential waxy barriers on the hypocotyl surface [25]. Both treatments improved callus formation along the hypocotyl, resembling the morphology observed in *A. thaliana* and *C. wallichii* (Supplementary Fig. S18a, d). However, these treatments alone did not significantly improve shoot regeneration in Westar, likely due to the formation of ineffective callus. Indeed, when combined with U0126 treatment, permeability-enhanced Westar calli became more slender and exhibited significantly improved regeneration efficiency (Supplementary Fig. S18c). Importantly, similar treatments also promoted shoot regeneration in ZS11 and Tapidor (Supplementary Fig. S18e, g).

We further conducted regeneration experiments on three cultivated tomato (*Solanum lycopersicum*) varieties: Alisa Craig (AC), M82, and Micro-Tom (MT) (Supplementary Fig. S19a–f). Under current protocols, all three varieties exhibited comparable shoot regeneration capacities (Supplementary Fig. S19a, c, e). Notably, shoots exclusively formed at the wound sites, leaving the middle portion of the explant underutilized—a phenomenon reminiscent of the previously observed behavior in the rapeseed variety Westar.

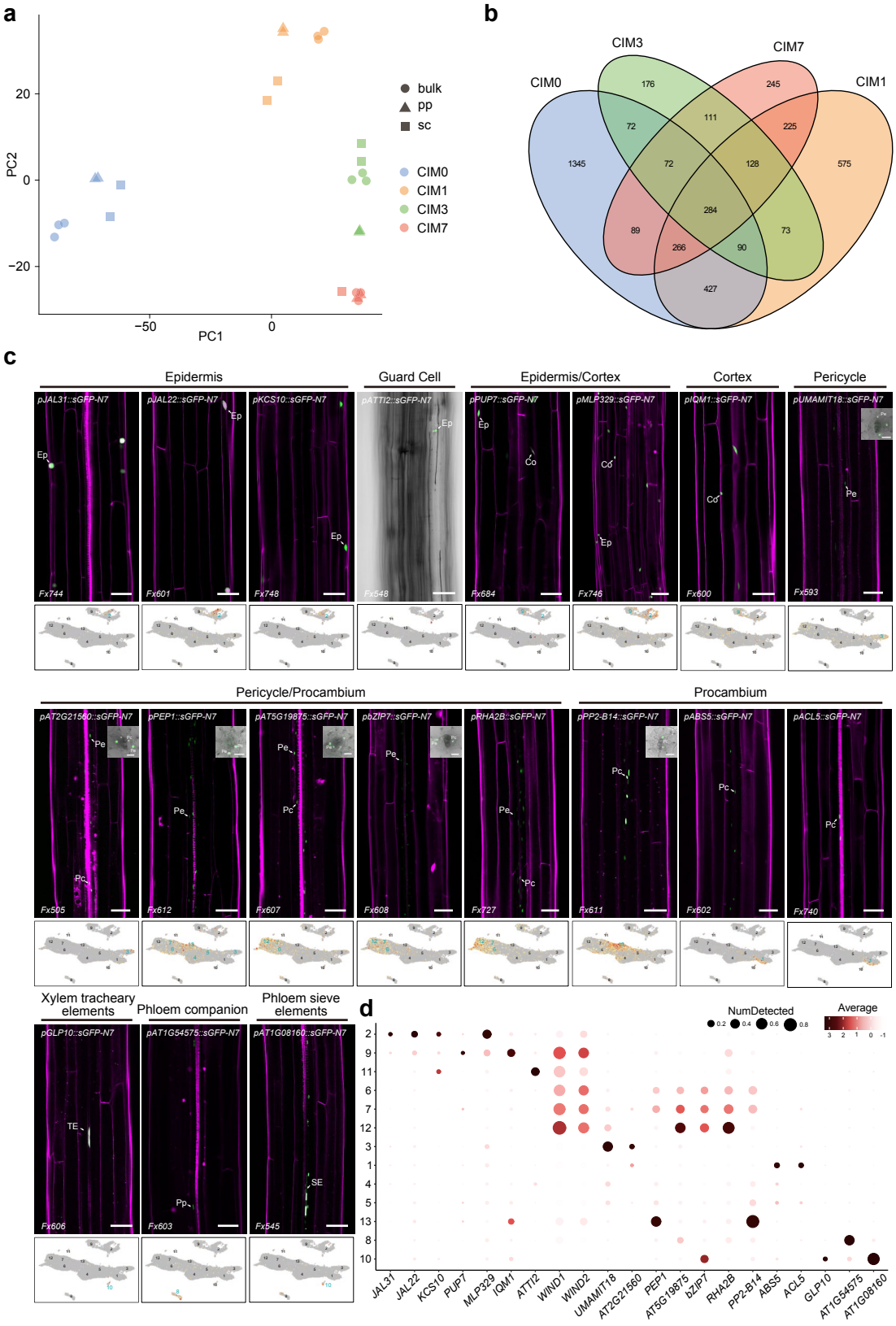
To address this, we applied squeeze or n-hexane pretreatments to tomato hypocotyl explants before culturing them on the CIM. However, n-hexane pretreatment proved toxic to all tomato varieties, drastically reducing callus induction and shoot regeneration efficiency (data not shown). Conversely, the squeeze pretreatment promoted extensive callus formation along the entire hypocotyls and significantly enhanced shoot regeneration capacities across all varieties (Supplementary Fig. S19b, d, f). Unfortunately, the addition of U0126 did not further enhance regeneration capacities (Supplementary Fig. S19a, c, e). A plausible explanation for this is that the squeeze treatment alone may have synchronized callus development in tomatoes, mimicking the effects of U0126 on *A. thaliana*.

Next, we evaluated the method on two *Solanum pimpinellifolium* varieties, LA1589 and LA1781, the wild ancestors of cultivated tomatoes. Consistent with findings in rapeseed and cultivated tomatoes, U0126 alone had a minor promoting effect on the shoot regeneration efficiency of LA1589 and LA1781 (Supplementary Fig. S19g, i). However, squeeze pretreatment significantly enhanced callus formation on the CIM and promoted shoot regeneration on the SIM in both wild varieties (Supplementary Fig. S19h, j).

Finally, we evaluated U0126 in *Medicago sativa*. The application of U0126 alone could enhance shoot regeneration efficiency to some extent (Supplementary Fig. S20a–c). Although the squeeze pretreatment by itself does not promote regeneration (Supplementary Fig. S20d–f), its combination with U0126 significantly enhanced shoot regeneration (Supplementary Fig. S20g).

Taken together, these findings highlight a fundamental distinction in callus formation and shoot regeneration potential across species. Explants like *A. thaliana* and *C. wallichii*, which readily form callus, tend to produce a higher proportion of ineffective callus tissue. In contrast, explants from species such as rapeseed and cultivated or wild tomatoes, which are less prone to callus formation, typically generate effective, pluripotent callus tissue more synchronously following squeeze pretreatment. For the former group, U0126 facilitates synchronized callus development, reducing ineffective callus regions and enhancing shoot regeneration.

Supplementary Figures



Supplementary Fig. S1. Assessment of callus cell atlas data and analyses of the cell atlas at CIM0.

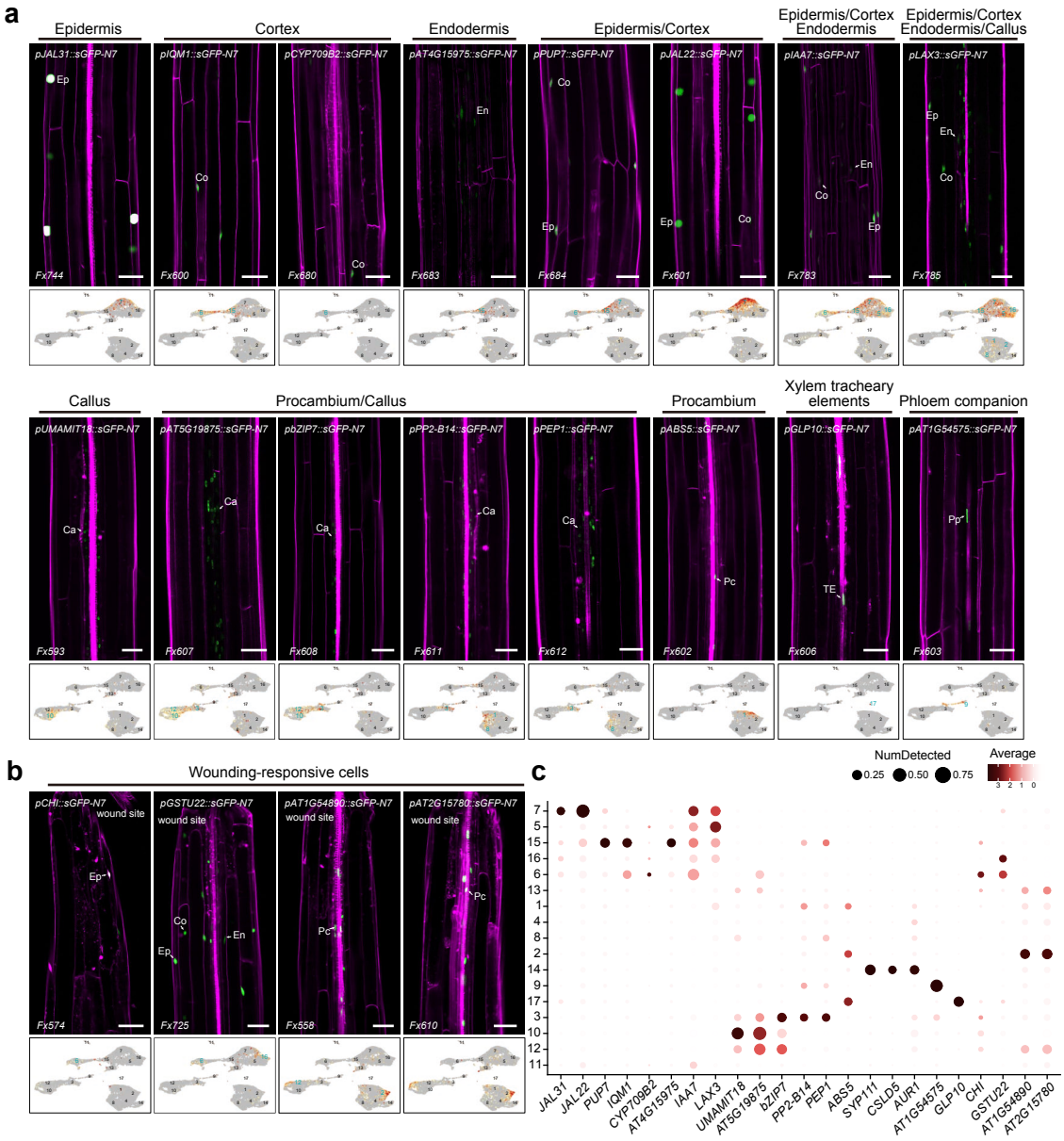
a PCA plot showing RNA-sequencing data of the calli at CIM0 to CIM7. bulk, bulk RNA-seq; pp: protoplast RNA-seq; sc: pseudo-bulk scRNA-seq.

b Venn diagram showing the intersection of protoplast-responsive genes at CIM0, 1, 3, and 7. The numbers of genes are given.

c Representative images showing the expression pattern of the reporters (nuclei-localized GFP) used for cell cluster annotations at CIM0. Co: cortex; Ep: epidermis; Pc: procambium; Pe: pericycle; Pp: phloem companion cells; SE: phloem sieve elements; TE: xylem tracheary cells. The expression pattern of each gene in the atlas is shown by the UMAP (Fig. 1a) at the bottom of each panel. The number of highly enriched cell clusters for each gene in the UMAP is highlighted in bold and cyan. Cell outlines were stained with propidium iodide (magenta), and white arrows indicate green GFP signals. Scale bars, 50 μm for longitudinal images and 10 μm for transverse images.

d Dot plot showing the enrichment of marker genes in each cell cluster at CIM0. The color of the dots represents the scaled average gene expression level, while the size of the dots indicates the proportion of cells in which the gene was detected. Y-axis: cell clusters in Fig. 1a; X-axis: representative genes.

The binary construct number (*FxNNN*) corresponding to each reporter line is provided at the bottom left corner of the image. See also Supplementary Table S1.



Supplementary Fig. S2. Analyses of the cell atlas at CIM1.

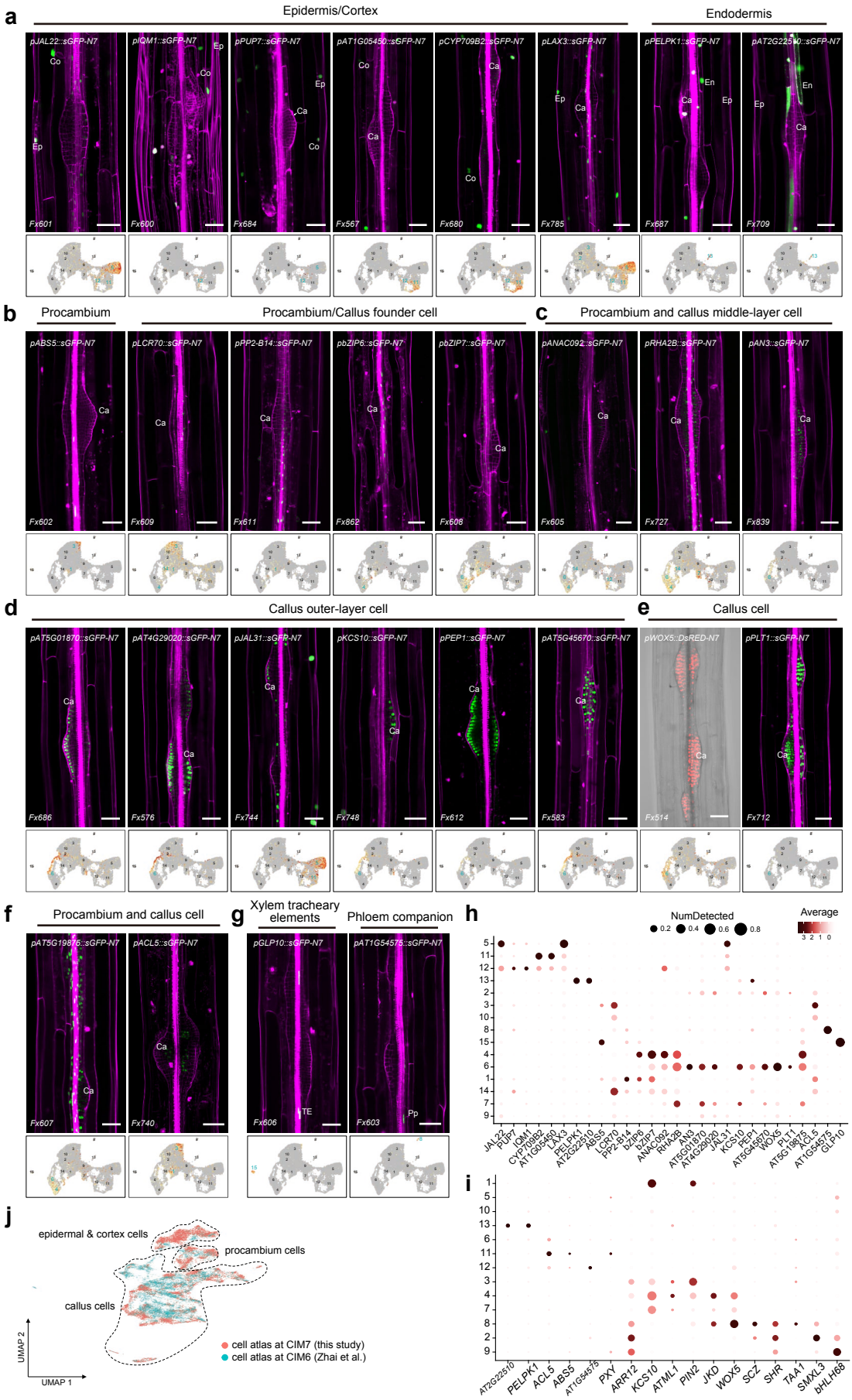
a Representative images showing the expression pattern of the reporters (nuclei-localized GFP) used for cell cluster annotations at CIM1. Ca: callus cells; Co: cortex; Ep: epidermis; Pc: procambium; Pe: pericycle; Pp: phloem companion cells; SE: phloem sieve elements; TE: xylem tracheary cells. The expression pattern of each gene in the atlas at CIM1 is shown by the UMAP (Fig. 1b) at the bottom of each panel. The number of highly enriched cell clusters for each gene in the UMAP is highlighted in bold and cyan. Cell outlines were stained with propidium iodide (magenta), and white arrows indicate green GFP signals. Scale bars, 50 μm.

b Representative images showing the expression pattern of the reporters (nuclei-localized GFP) for

wounding-responsive genes at CIM1. Scale bars, 50 μm.

c Dot plot showing the enrichment of marker genes in each cell cluster at CIM1. The color of the dots represents the scaled average gene expression level, while the size of the dots indicates the proportion of cells in which the gene was detected. Y-axis: cell clusters in Fig. 1b; X-axis: representative genes.

The binary construct number (*FxNNN*) corresponding to each reporter line is provided at the bottom left corner of the image. See also Supplementary Table S1.


a
Epidermis/Cortex
Endodermis
pJAL22::sGFP-N7
pQM1::sGFP-N7
pPUP7::sGFP-N7
pAT1G05450::sGFP-N7
pCYP709B2::sGFP-N7
pLAX3::sGFP-N7
pPELPK1::sGFP-N7
pAT2G22510::sGFP-N7
b
Procambium
Procambium/Callus founder cell
pABS5::sGFP-N7
pLCR70::sGFP-N7
pPP2-B14::sGFP-N7
pbZIP6::sGFP-N7
pbZIP7::sGFP-N7
c
Procambium and callus middle-layer cell
pANAC092::sGFP-N7
pRHA2B::sGFP-N7
pAN3::sGFP-N7
d
Callus outer-layer cell
pAT5G01870::sGFP-N7
pAT4G29020::sGFP-N7
pJAL31::sGFP-N7
pKCS10::sGFP-N7
pPEP1::sGFP-N7
pAT5G45670::sGFP-N7
e
Callus cell
pWOX5::DsRED-N7
pPLT1::sGFP-N7
f
Procambium and callus cell
pAT5G19876::sGFP-N7
pACL5::sGFP-N7
g
Xylem tracheary elements
Phloem companion
pGLP10::sGFP-N7
pAT1G54575::sGFP-N7
h
NumDetected
Average
i
j
epidermal & cortex cells
procambium cells
callus cells
UMAP 2
UMAP 1
cell atlas at CIM7 (this study)
cell atlas at CIM6 (Zhai et al.)

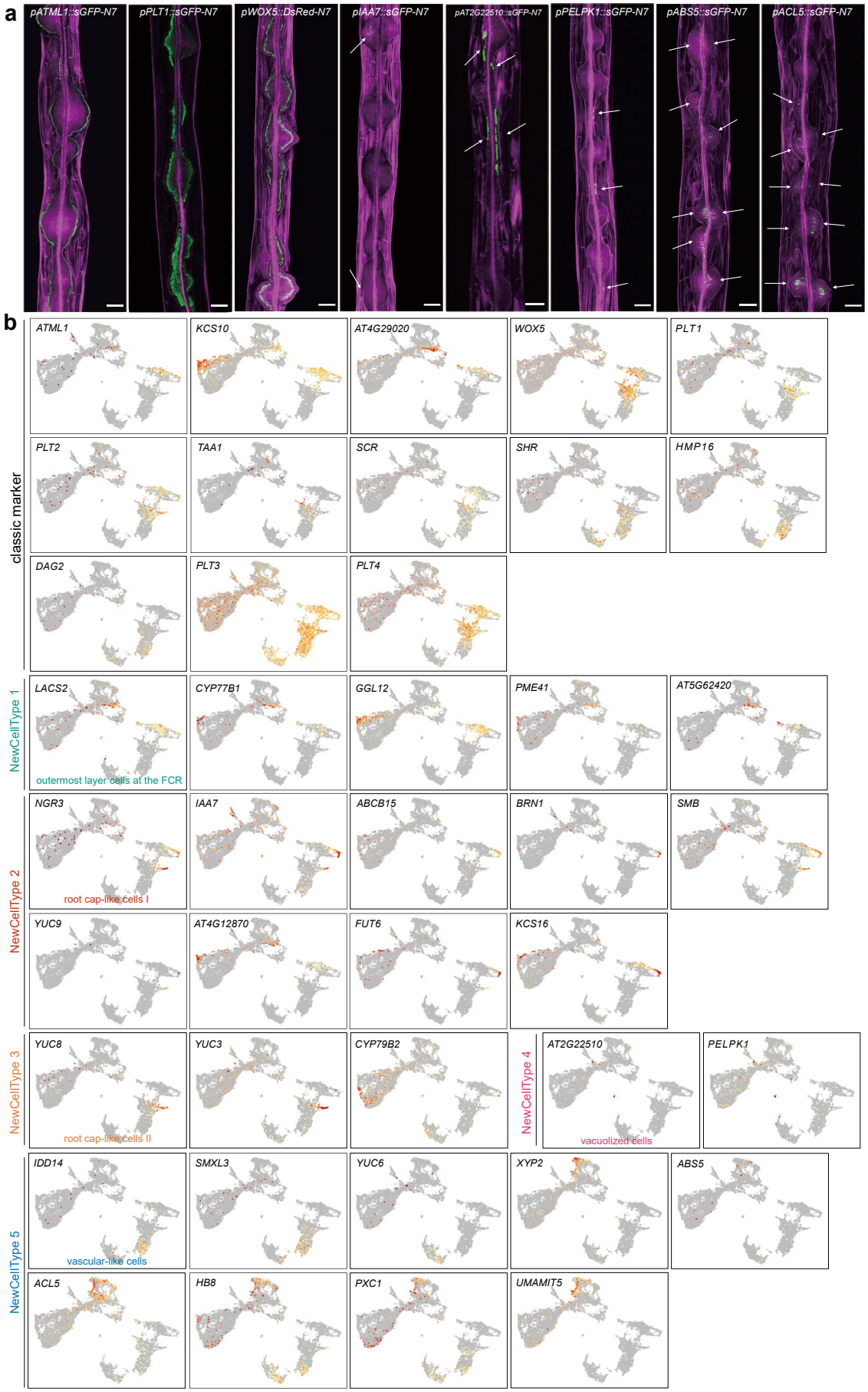
Supplementary Fig. S3. Analyses of the cell atlas at CIM3 and CIM7.

a–g Representative images showing the expression pattern of the reporters (nuclei-localized GFP) used for annotating Epidermis/Cortex cells (**a**), Procambium/Callus founder cells (**b**)[30], Procambium/Middle-layer callus cells (**c**), Outer-layer callus cells (**d**), Callus cells (**e**), Procambium/Callus cells (**f**), and TE/Phloem companion cells (**g**) at CIM3. Ca: callus cells; Co: cortex; Ep: epidermis; Pc: procambium; Pe: pericycle; Pp: phloem companion cells; SE: phloem sieve elements; TE: xylem tracheary cells. The expression pattern of each gene in the atlas at CIM3 is shown by the UMAP (Fig. 1c) at the bottom of each panel. The number of highly enriched cell clusters for each gene in the UMAP is highlighted in bold and cyan. Cell outlines were stained with propidium iodide (magenta). Scale bars, 50 μm.

h, i Dot plot showing the enrichment of marker genes in each cell cluster at CIM3 (**h**) and CIM7 (**i**). The color of the dots represents the scaled average gene expression level, while the size of the dots indicates the proportion of cells in which the gene was detected. Y-axis: cell clusters in Fig. 1c (**h**) and cell clusters in Fig. 1d (**i**); X-axis: representative genes.

j Integration of the callus atlas at CIM7 (this study) with the atlas at CIM6 (Zhai et al.) [11]. Please note that the epidermis and cortex of the explants were manually removed by Zhai et al. [11].

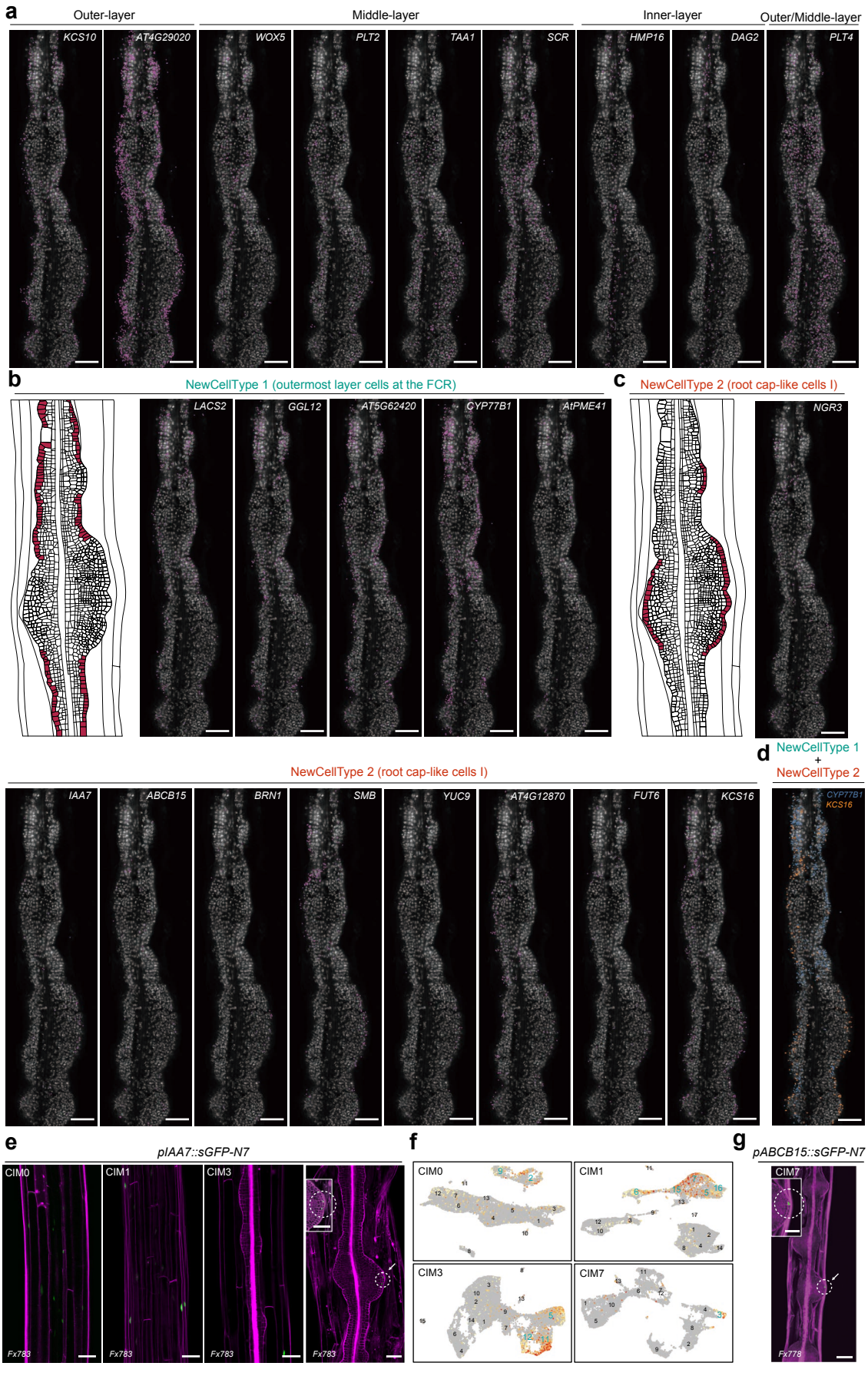
The binary construct number (*FxNNN*) corresponding to each reporter line is provided at the bottom left corner of the image. See also Supplementary Table S1.


a
pATML1::sGFP-N7
pPLT1::sGFP-N7
pWOX5::DsRed-N7
pIAA7::sGFP-N7
pAT2G22510::sGFP-N7
pPELPK1::sGFP-N7
pABS5::sGFP-N7
pACL5::sGFP-N7
b
classic marker
ATML1
KCS10
AT4G29020
WOX5
PLT1
PLT2
TAA1
SCR
SHR
HMP16
DAG2
PLT3
PLT4
NewCellType 1
LACS2
CYP77B1
GGL12
PME41
AT5G62420
outermost layer cells at the FCR
NewCellType 2
NGR3
IAA7
ABCB15
BRN1
SMB
root cap-like cells I
YUC9
AT4G12870
FUT6
KCS16
NewCellType 3
YUC8
YUC3
CYP79B2
root cap-like cells II
NewCellType 4
AT2G22510
PELPK1
vacuolized cells
NewCellType 5
IDD14
SMXL3
YUC6
XYP2
ABS5
vascular-like cells
ACL5
HB8
PXC1
UMAMIT5

Supplementary Fig. S4. Analyses of reporter lines at CIM7.

a Representative images showing the expression patterns of the reporters (nuclei-localized GFP or DsRed) for outer-layer (*ATML1*), middle-layer (*PLT1* and *WOX5*), and other specific regions (*IAA7*, *AT2G22510*, *PELPK1*, *ABS5*, and *ACL5*) in the callus at CIM7. To demonstrate the heterogeneity of the callus tissue in a direction parallel to the vascular bundles of the explant, the image is a composite taken under a 20× objective lens. White arrows indicate specific expression regions within the callus at CIM7. Cell outlines were stained with SR2200 (magenta). Scale bars, 100 μm.

b UMAPs showing the expression patterns of the marker genes for classic and new cell types identified in this study. Genes are arranged according to their spatially resolved expression patterns. The atlas is the same in Fig. 1d.


a
Outer-layer
Middle-layer
Inner-layer
Outer/Middle-layer
KCS10
AT4G29020
WOX5
PLT2
TAA1
SCR
HMP16
DAG2
PLT4
b
NewCellType 1 (outermost layer cells at the FCR)
LACS2
GGL12
AT5G62420
CYP77B1
AtPME41
c
NewCellType 2 (root cap-like cells I)
NGR3
d
NewCellType 1
+
NewCellType 2
NewCellType 2 (root cap-like cells I)
IAA7
ABCB15
BRN1
SMB
YUC9
AT4G12870
FUT6
KCS16
CYP77B1
KCS16
e
pIAA7::sGFP-N7
CIM0
CIM1
CIM3
Fx783
f
CIM0
CIM1
CIM3
CIM7
g
pABCB15::sGFP-N7
CIM7
Fx778

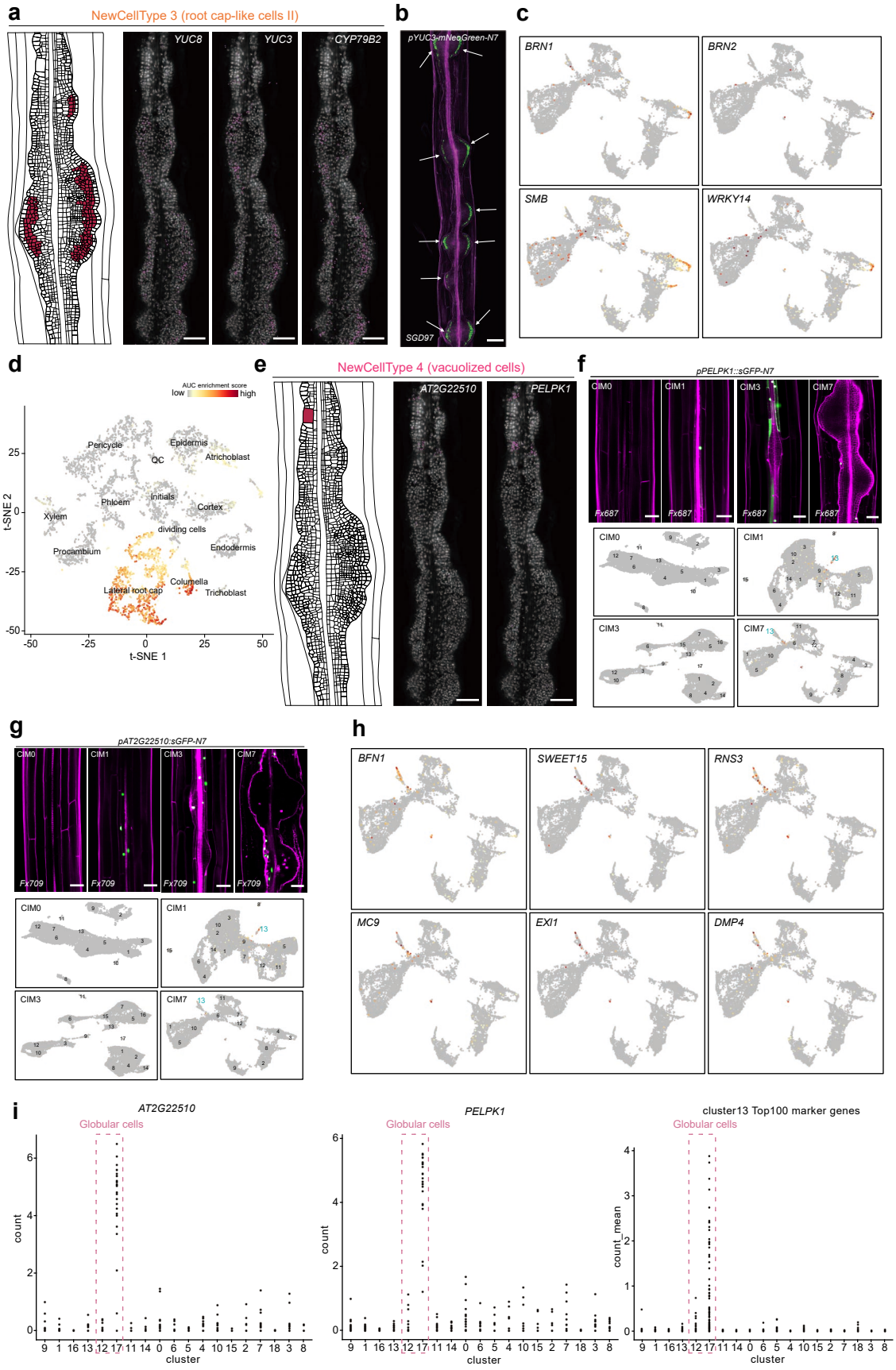
Supplementary Fig. S5. Spatial transcriptome analyses of new cell types (N1 and N2) at CIM7.

a Expression patterns of classic cell type marker genes at CIM7 revealed by spatial transcriptomics. The purple dots represent the regions of gene expression. Please note that *PLT4*/*BBM* is primarily expressed in the outer and middle layers of the callus. Scale bars, 50 μm. See also Fig. 2a.

b–d Expression patterns of marker genes for N1 (**b**), N2 (**c**), and N1+N2 (**d**) at CIM7 revealed by spatial transcriptomics. Schematic diagrams of the spatial distribution for new cell types (magenta) are given. Please note that that transcripts of N1 marker gene *CYP77B1* and the N2 marker gene *KCS16* are not co-localized (**d**). Scale bars, 50 μm.

e, f Expression pattern of *IAA7* revealed by sGFP reporter line (**e**) and UMAPs (**f**). The number of highly enriched cell clusters for each gene in the UMAP is highlighted in bold and cyan. Cell outlines were stained with propidium iodide (magenta). Please note that the image showing the expression pattern of *IAA7* at CIM1 is the same as the one in Supplementary Fig. S2a. The expression pattern of *IAA7* at N2 is illustrated using a localized zoom-in, highlighted with dashed circles. Scale bars in (**e**), 50 μm.

g Expression pattern of the N2 marker gene *ABCB15* at CIM7. White arrow indicates the region where the *ABCB15* reporter line was expressed. Please note that *ABCB15* was also expressed in the inner cells of the ACR. Cell outlines were stained with SR2200 (magenta). To demonstrate the heterogeneity of the callus tissue in a direction parallel to the vascular bundles of the explant, the image is a composite taken under a 20× objective lens. The expression pattern of *ABCB15* at N2 is depicted by a localized zoom-in, highlighted with dashed circles. Scale bars, 100 μm in the main images and 50 μm in the magnified image.



Supplementary Fig. S6. Spatial transcriptome analyses of new cell types (N3 and N4) at CIM7.

a Expression patterns of three marker genes for N3 at CIM7 revealed by spatial transcriptomics. Schematic diagram of the spatial distribution for N3 (magenta) is given. The purple dots represent the regions of gene expression. Scale bars, 50 μm.

b Expression pattern of the reporter line for the N3 marker gene *YUC3* at CIM7. White arrows indicate the region where the *YUC3* reporter line was expressed. Cell outlines were stained with SR2200 (magenta). To demonstrate the heterogeneity of the callus tissue in a direction parallel to the vascular bundles of the explant, the image is a composite taken under a 20× objective lens. Scale bars, 100 μm.

c UMAPs showing the reported root cap genes at CIM7. Please note that all these genes are primarily enriched in N3 (Supplementary Table S1).

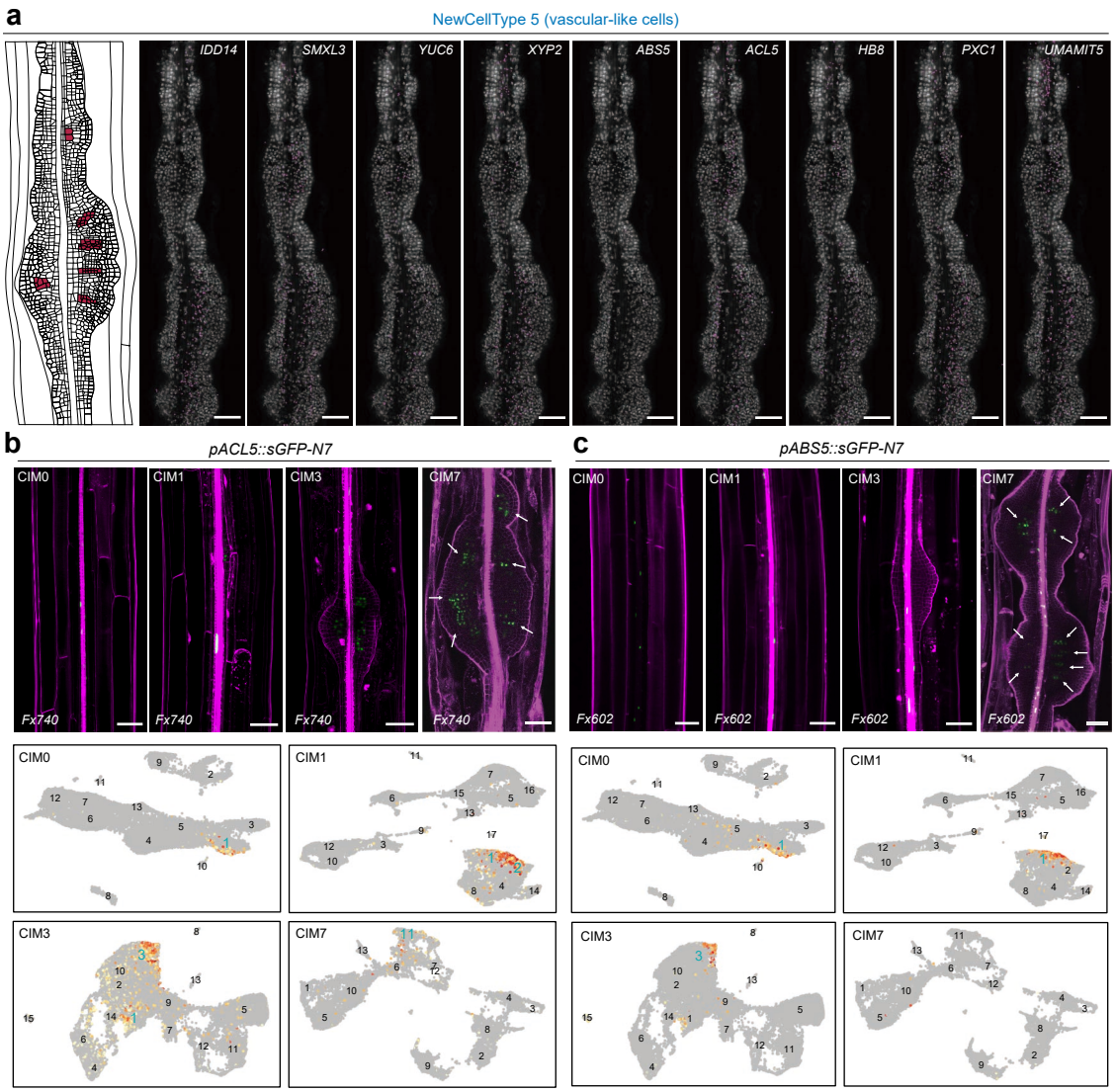
d *t*-SNE plot showing the expression pattern of the marker gene set of cluster 3 at CIM7 in the *A. thaliana* root cell atlas [26]. Color bar represents the degree of enrichment. AUCell was used to calculate the enrichment scores of the gene set in individual cells.

e Expression patterns of two marker genes for N4 at CIM7 revealed by spatial transcriptomics. Schematic diagram of the spatial distribution for N4 (magenta) is given. The purple dots represent the regions of gene expression. Scale bars, 50 μm.

f, g Expression patterns of the N4 marker genes *PELPK1* (**f**) and *AT2G22510* (**g**). Cell outlines were stained with propidium iodide (magenta). The expression pattern of each gene in the atlas is shown by the UMAP at the bottom of each panel. The number of highly enriched cell clusters for each gene in the UMAP is highlighted in bold and cyan. Please note that the images showing the expression pattern of these two genes at CIM3 are the same as those in Supplementary Fig. S3a. Scale bars, 50 μm.

h UMAPs showing the expression patterns of reported senescence and death-related genes at CIM7. Please note that most of these genes are primarily enriched in cluster 13 (Fig. 1d).

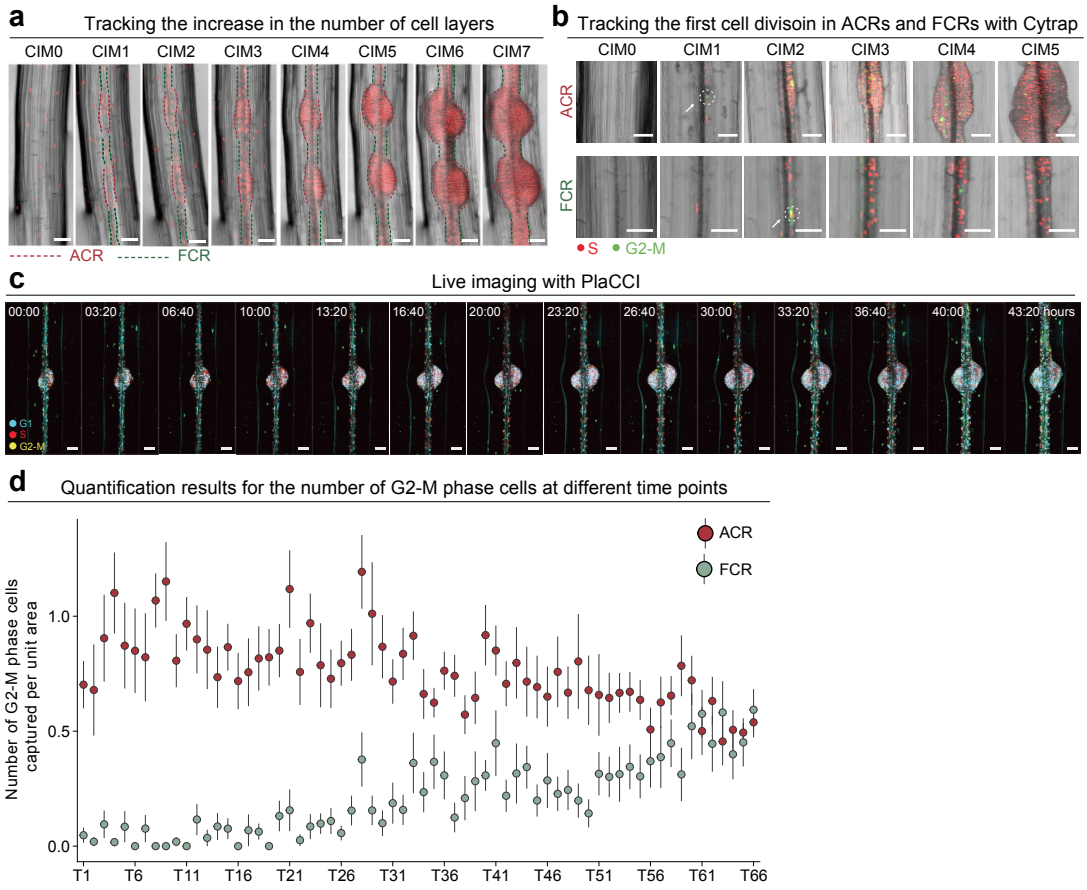
i Expression trends of *AT2G22510*, *PELPK1*, and the top 100 cluster 13 marker genes in the cell atlas generated by Ogura et al.. X-axis, cell clusters in Ogura et al. callus cell atlas at SIM6. The pink dashed boxes represent the cell clusters annotated as "highly expanded globular cells" by Ogura et al. [13].



Supplementary Fig. S7. Spatial transcriptome analyses of N5 at CIM7.

a Expression patterns of nine marker genes for N5 at CIM7 revealed by spatial transcriptomics. Schematic diagram of the spatial distribution for N5 (magenta) is given on the left. The purple dots represent the regions of gene expression. Scale bars, 50 μm.

b, c Expression patterns of the reporter lines for the N5 marker gene *ACL5* (**b**) and *ABS5* (**c**). Cell outlines were stained with propidium iodide (magenta). The expression pattern of each gene in the atlas is displayed by UMAP at the bottom of each panel. The number of highly enriched cell clusters for each gene in the UMAP is highlighted in bold and cyan. Arrows indicate the striped patterns of *ACL5* (**b**) and *ABS5* (**c**) in callus cells. Scale bars, 50 μm.



Supplementary Fig. S8. Supporting data for tracking cell division patterns of ACRs and FCRs.

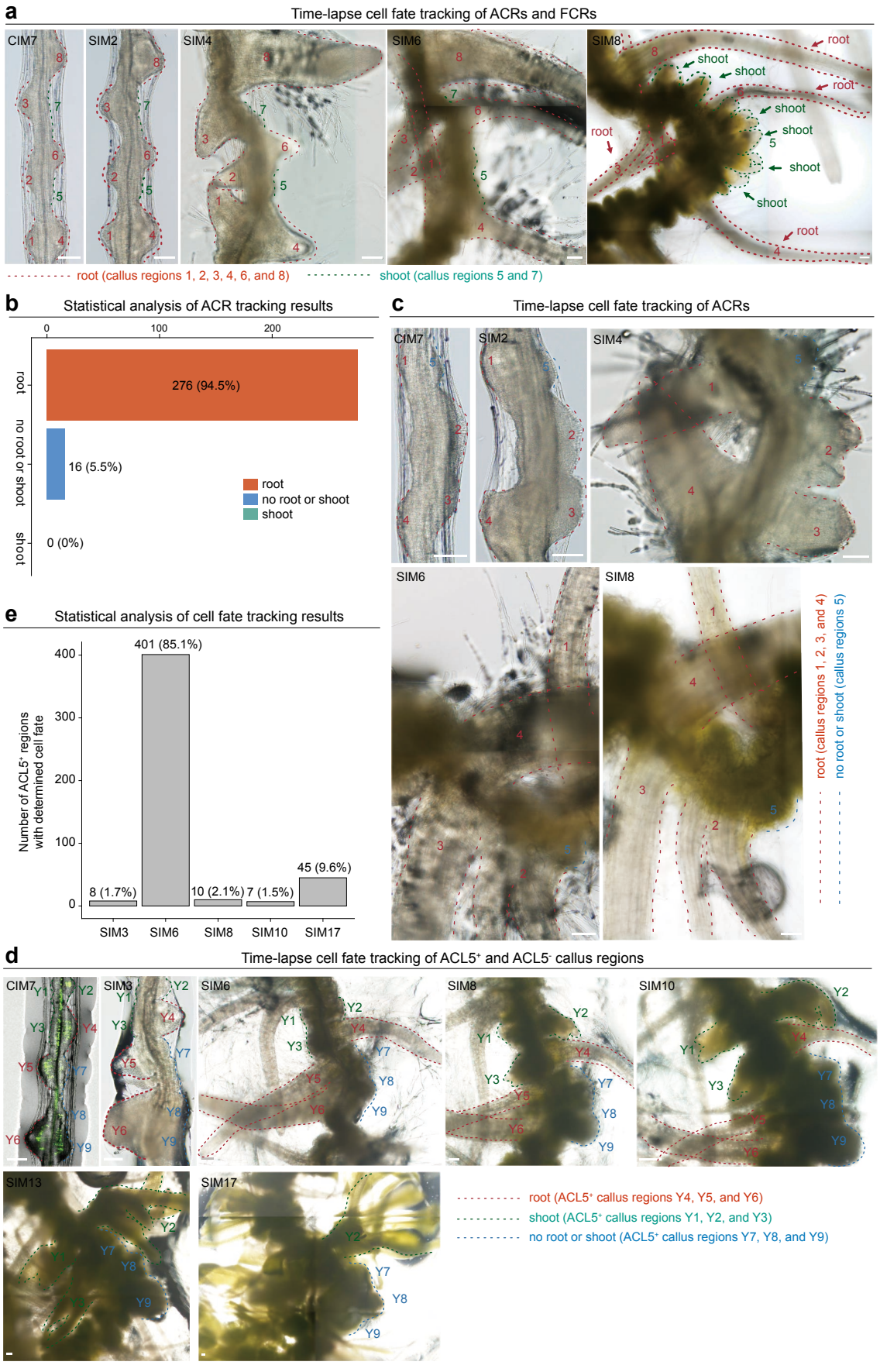
a Quantification of the rate of increase in cell layer number in ACRs and FCRs was performed using a constitutive nuclear localization reporter line (*pAT2G18020:H2B-mCherry*) [27]. Representative callus images are shown, with ACRs and FCRs outlined by red and green dashed lines, respectively. Calli were imaged daily from CIM0 to CIM7. Eight explants were analyzed and quantified. *n* represents the number of tracked callus regions (n = 104 for ACRs and n = 111 for FCRs). Quantitative analyses are presented in Fig. 2d, e.

b Tracking of the first cell division in corresponding pericycle cells of ACRs and FCRs was performed using the dual-color Cytrap system [28]. The first cells entering the G2–M phase (*pCYCB1::CYCB1-GFP*, green) in each region are circled, while cells undergoing the S–G2 transition (*pHTR2::CDT1a (C3)-RFP*, red) are also indicated. Six explants were analyzed, with n = 120 for ACRs and n = 128 for FCRs. Quantification results are provided in Fig. 2f.

c, d Live imaging using PlaCCI [29] was conducted from CIM3 to CIM5 to track cell division dynamics

in ACRs and FCRs. A total of 66 time-lapse rounds (T1–T66) were acquired at 40-minute intervals. Distinct fluorescence signals were used to distinguish G1, S, and G2–M cell cycle phases. Representative images and quantification of G2–M phase cells per unit area over time are shown in panels (**c**) and (**d**), respectively. *n* represents the number of tracked callus regions (*n* = 11 callus regions for ACRs and *n* = 15 for FCRs). See also Supplementary Video S1.

Scale bars in (**a–c**), 50 μm.



Supplementary Fig. S9. Supporting data for cell fate tracking of ACRs.

a Time-lapsed cell fate tracking of ACR and FCR using wild-type explants under white-light. Representative callus images are shown, with ACRs and FCRs marked by red and green dashed lines, respectively. Images display eight representative regions in a callus, tracked every two days from CIM7 to SIM8. Shoots and roots at CIM8 are indicated.

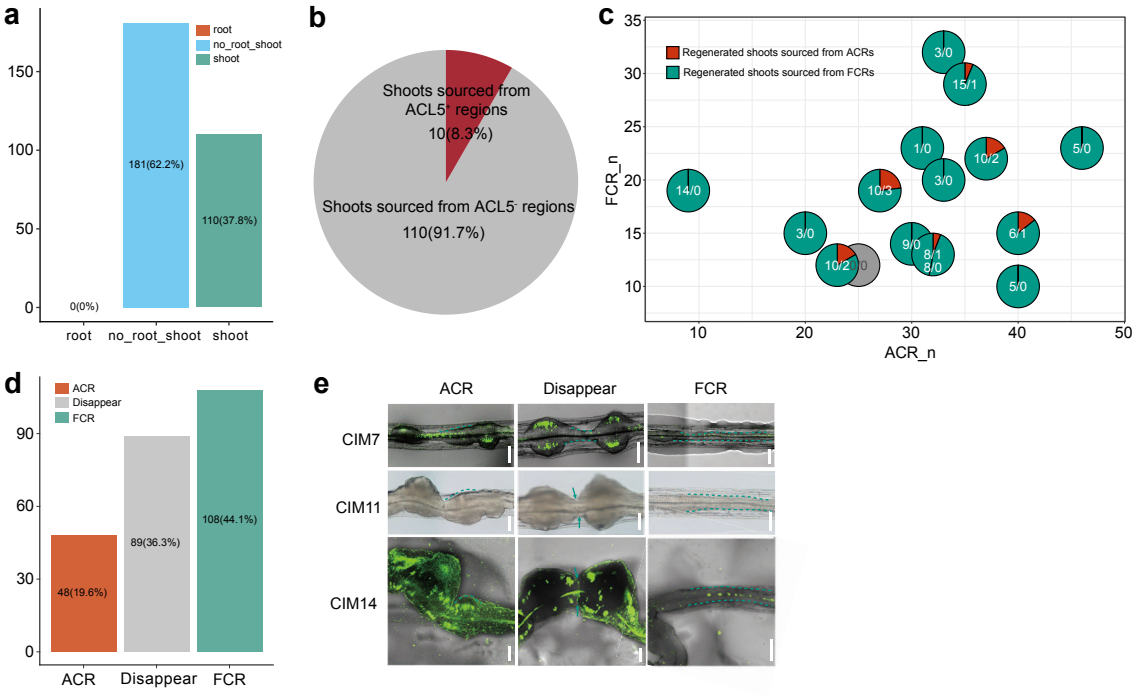
b Statistical analysis of cell fate tracking results in (**a**). The final cell fate of ACRs was classified into three categories: root, no root or shoot, and shoot. The percentage of each category is shown. Data are from three independent experiments. In total, 292 ACRs from 19 callus explants were tracked and quantified.

c Time-lapsed cell fate tracking of ACRs using wild-type explants under white-light. Red dashed lines mark the regions that will eventually develop into roots, while the blue dashed lines label those that will not transform into either shoots or roots.

d Time-lapse tracing of $ACL5^{+}$ regions was performed from CIM7 to SIM17 using the ACL5 reporter line. Red and green dashed lines mark regions that ultimately develop into roots or shoots, respectively, while blue dashed lines indicate regions that do not give rise to either organ. $ACL5^{+}$ cells (green) were analyzed at CIM7. Regions Y4–Y6 are not shown at SIM13 and SIM17 as their cell fates had already been determined.

e Statistical analysis of $ACL5^{+}$ regions with defined cell fates across time points revealed that most fates were established by SIM6. In total, 471 $ACL5^{+}$ regions were tracked.

Scale bars in (**a**, **c**, **d**), 100 μm.



Supplementary Fig. S10. Supporting data for cell fate tracking of the FCRs.

a Statistical analysis of cell fate tracking results of FCRs. ACRs and FCRs were simultaneously tracked. Data are from three independent experiments. In total, 291 FCR regions (i.e., non-ACL5-labeled regions) from 16 explants were tracked. The final fates of FCRs were classified into three categories: root, no root or shoot, and shoot. The percentage for each category is shown. See cell fate tracking results of ACRs in Fig. 3e.

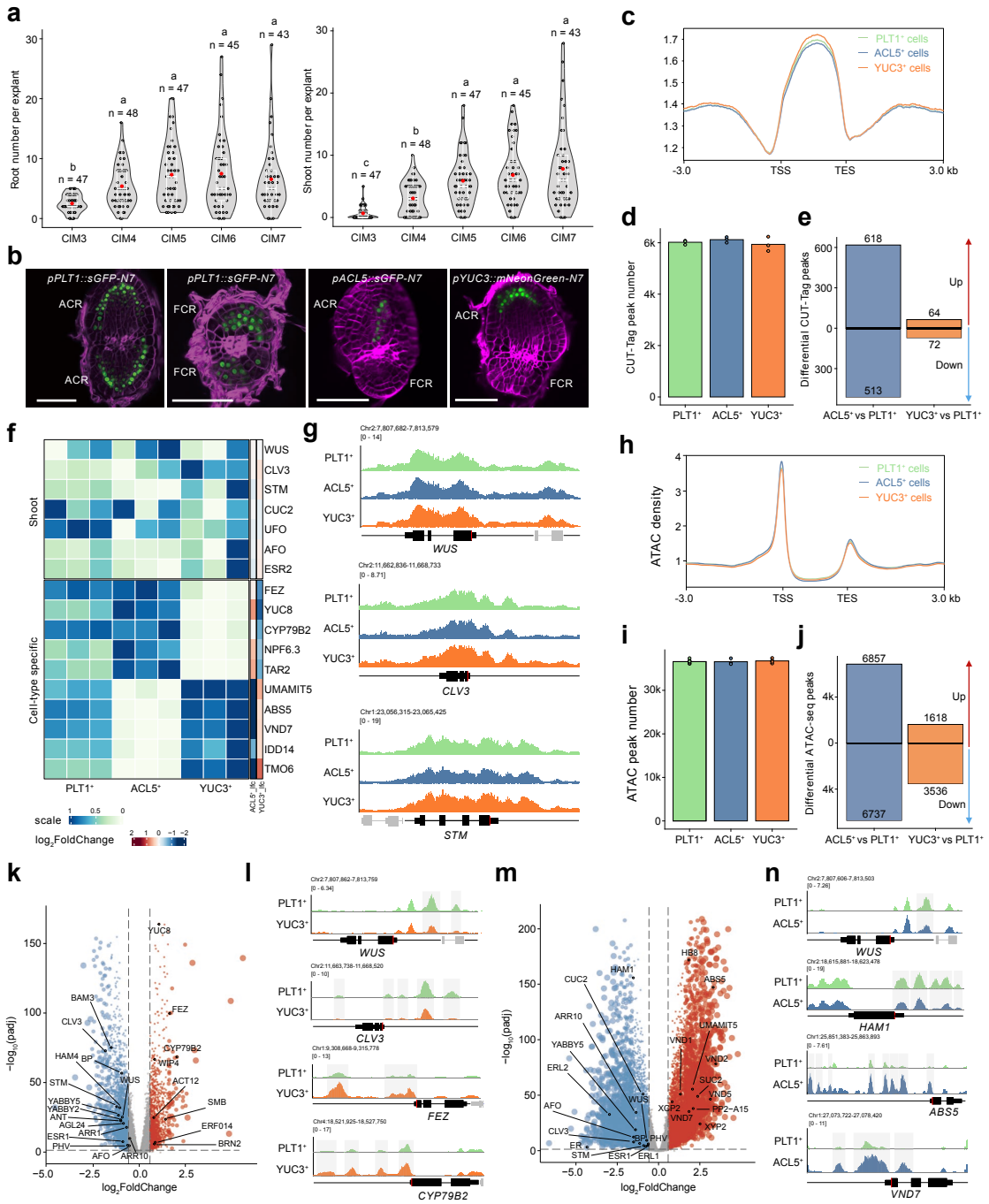
b Statistical summary of the source of regenerated shoots. Please note that only 10% of regenerated shoots were derived from the ACL5^{+} regions.

c The number of regenerated shoots sourced from ACRs or FCRs. In total, 16 explants were examined. Each circle represents the quantification results for one explant (sourced from FCRs/source from ACRs).

d Statistical summary of long-term cell fate tracking results. The ACL5 reporter line was used. The FCRs were defined at CIM7 and the cell fates were tracked until CIM14. Data are from three independent experiments. In total, 245 FCR regions from 18 explants were tracked. The final fates of FCRs were classified into three categories: ACR, Disappear and FCR. The percentage distribution of each category is shown.

e Representative images illustrating cell fate tracking results (**d**). Each category displays one tracking

result, with images taken at CIM7, CIM11, and CIM14. The green dashed lines indicate FCRs, and the green arrows point to the disappearing FCRs due to compression caused by the development of the surrounding two ACRs. Scale bars, 100 μm.



Supplementary Fig. S11. Supporting data for differential cell fate of ACRs and FCRs.

a The number of regenerated roots and shoots from the wild-type (Col-0) calli cultured on the CIM for different periods (3 to 7 days). The calli at CIM3-7 were transferred to the SIM and regeneration phenotype was quantified at SIM16. Callus counts are shown at the top of each column. Lowercase letters indicate statistically significant differences, as determined by one-way ANOVA with Tukey's multiple comparisons test.

b Expression patterns of *PLT1*, *ACL5*, and *YUC3* reporter lines were examined in transverse callus

sections at CIM7. Cell outlines were counterstained with propidium iodide (magenta). Scale bars, 50 μm.

c Genome-wide H3K27me3 distribution profiles were generated for PLT1$^+$, ACL5$^+$, and YUC3$^+$ cells.

d The total number of CUT&Tag-seq peaks per sample is shown, with three biological replicates per condition.

e Differential CUT&Tag-seq peak analysis was performed between PLT1$^+$ vs. YUC3$^+$ and PLT1$^+$ vs. ACL5$^+$ cells.

f A heatmap depicts genes with differential H3K27me3 levels. Notably, shoot-related genes (top cluster) exhibited no significant variation among PLT1$^+$, ACL5$^+$, and YUC3$^+$ cells. Notably, genes conferring root cap and vascular identities, including *FEZ*, *CYP79B2*, *ABS5*, and *VND7*, exhibited reduced H3K27me3 levels in the corresponding cells, which shows the reliability of CUT&Tag-seq data.

g IGV tracks show representative shoot-related loci (*WUS*, *CLV3*, and *STM*), with selected genes highlighted in black. Values in square brackets denote normalized read counts.

h Genome-wide ATAC-seq peak distributions were profiled for PLT1$^+$, ACL5$^+$, and YUC3$^+$ cells.

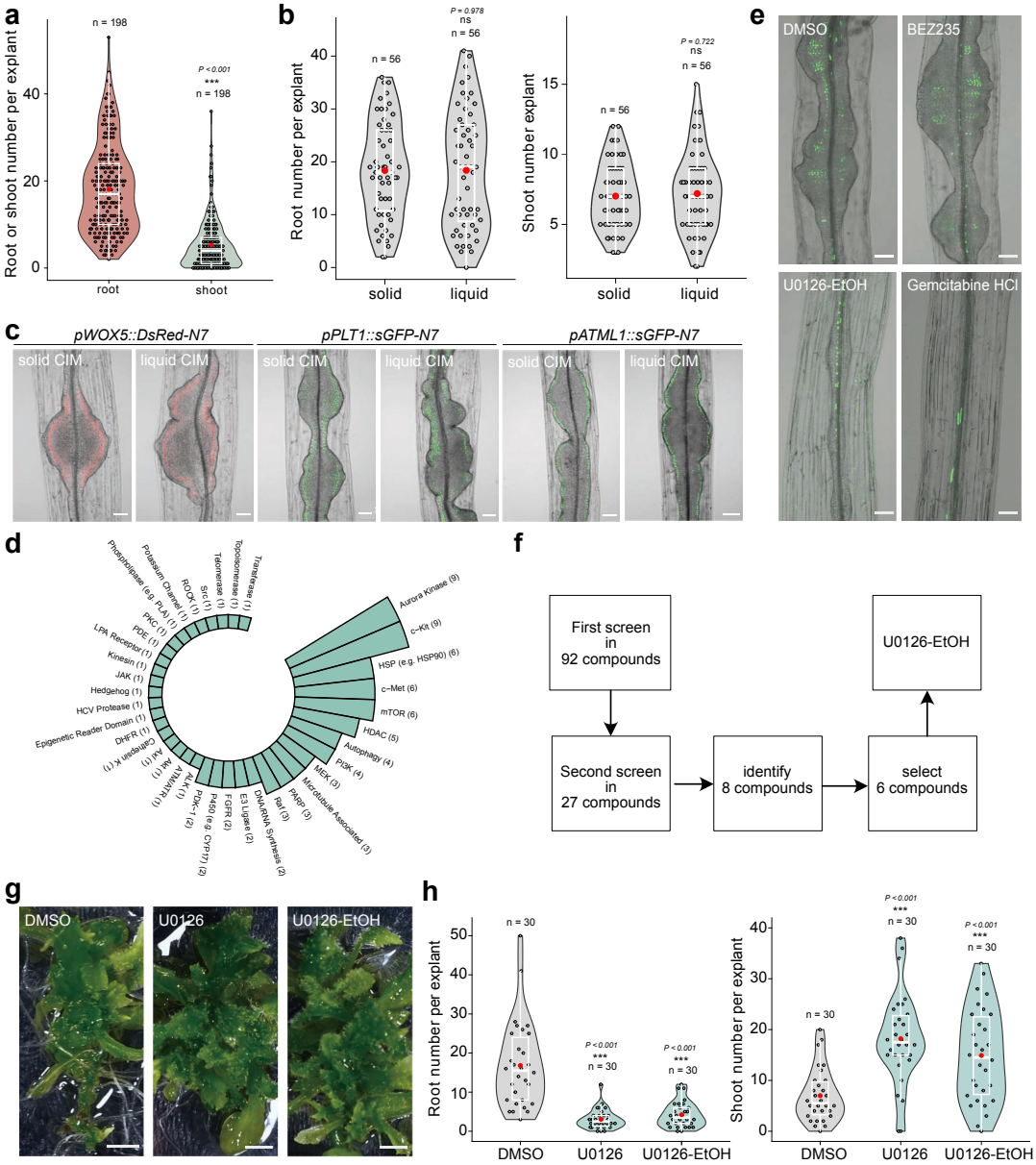
i Total ATAC-seq peak counts per sample are shown, with at least three biological replicates: $n = 7$ for PLT1$^+$, $n = 3$ for ACL5$^+$, and $n = 4$ for YUC3$^+$ cells.

j Numbers of differential ATAC-seq peaks were calculated between PLT1$^+$ vs. YUC3$^+$ and PLT1$^+$ vs. ACL5$^+$ cells.

k, m Volcano plots display differentially accessible genes between PLT1$^+$ and YUC3$^+$ (**k**), and PLT1$^+$ and ACL5$^+$ (**m**) cells.

l, n IGV plots illustrate representative loci showing differential chromatin accessibility in PLT1$^+$ vs. YUC3$^+$ (**l**) and PLT1$^+$ vs. ACL5$^+$ (**n**) cells. Differentially accessible regions are shaded, and normalized read counts are indicated in square brackets.

Thresholds in (**k–n**) were established at $padj < 0.05$ and absolute $\log_2$FoldChange > 0.58.



Supplementary Fig. S12. Supporting data for chemical screening.

a Violin plot illustrating the number of regenerated shoots and roots. The data are the same in Fig. 4b. The data are quantified at SIM16 and callus counts are shown at the top of each column. Medians (middle bars), quartiles (boxes), and 1.5× interquartile ranges (whiskers) are indicated. Red dots represent means. *n* represents the number of callus explants. Statistical analysis was conducted using a Student's *t*-test. *** $P < 0.001$.

b Comparison of regeneration efficiency under solid and liquid CIM conditions. The numbers of shoots and roots per explant were quantified at SIM16. *n* represents the number of callus explants. Statistical analysis was performed using a Student's *t*-test. ns, not significant.

c Expression patterns of representative reporters at CIM7 under solid and liquid CIM conditions. Scale bars, 50 μm.

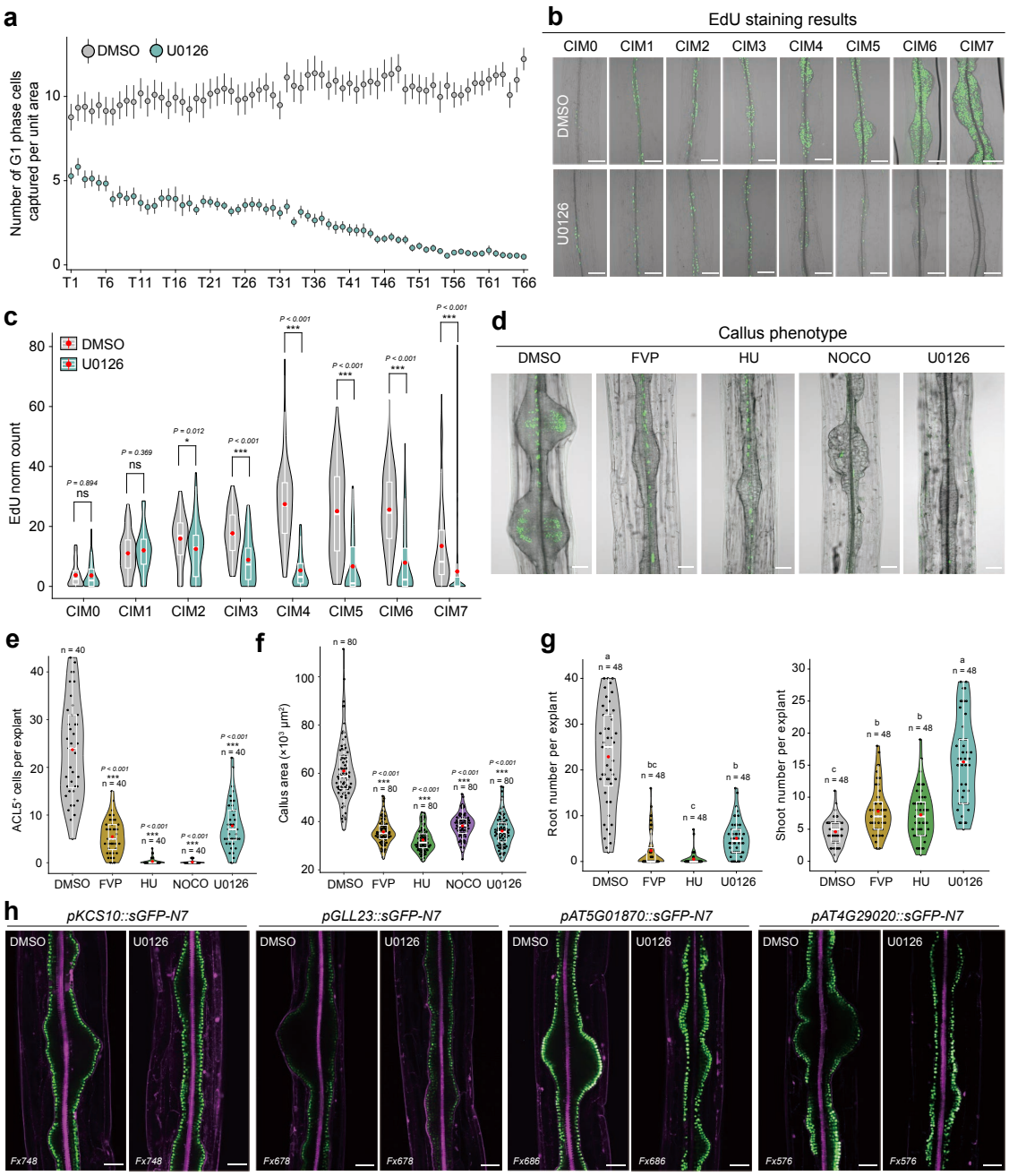
d Classification chart of the targets of 92 compounds used in this study. The number of compounds of each target is given in parentheses.

e Representative images showing the effect of candidate compounds on callus growth and the expression pattern of the *ACL5* reporter (green). The hypocotyls of the *pACL5::sGFP-N7* reporter line were used as explants. Please note that the three examples represent that, after compound treatment, the number of $ACL5^{+}$ cells either remains unchanged (BEZ235) or decreases (U0126-EtOH), and the callus does not proliferate (Gemcitabine HCl), respectively. Scale bars, 50 μm.

f Flowchart of the compound screening process. See Methods.

g Representative images illustrating the effect of U0126 and U0126-EtOH on shoot regenerative efficiency. Scale bars, 2 mm.

h Effects of U0126 and U0126-EtOH on regenerative efficiency. The number of regenerated roots (left) and shoots (right) was quantified at SIM16 and shown as violin plots. Callus counts are shown at the top of each column. Medians (middle bars), quartiles (boxes), and 1.5× interquartile ranges (whiskers) are indicated. Red dots represent means. *n* represents the number of callus explants. Statistical analysis was performed using one-way ANOVA with Tukey's multiple comparisons. *** $P < 0.001$.



Supplementary Fig. S13. Supporting data for the cellular mechanism of U0126.

a Time-lapse tracking of callus cell division from CIM3 to CIM5 was performed using live imaging with PlaCCI. The number of G1-phase cells per unit area at each time point is shown. A total of 66 imaging rounds (T1–T66) were conducted at 40-minute intervals. Sample sizes were n = 18 callus regions for DMSO and n = 17 for U0126. See also Fig. 5h; Supplementary Video S2 and S3.

b Representative EdU staining of mock- and U0126-treated calli from CIM0 to CIM7. Scale bars, 100 μm.

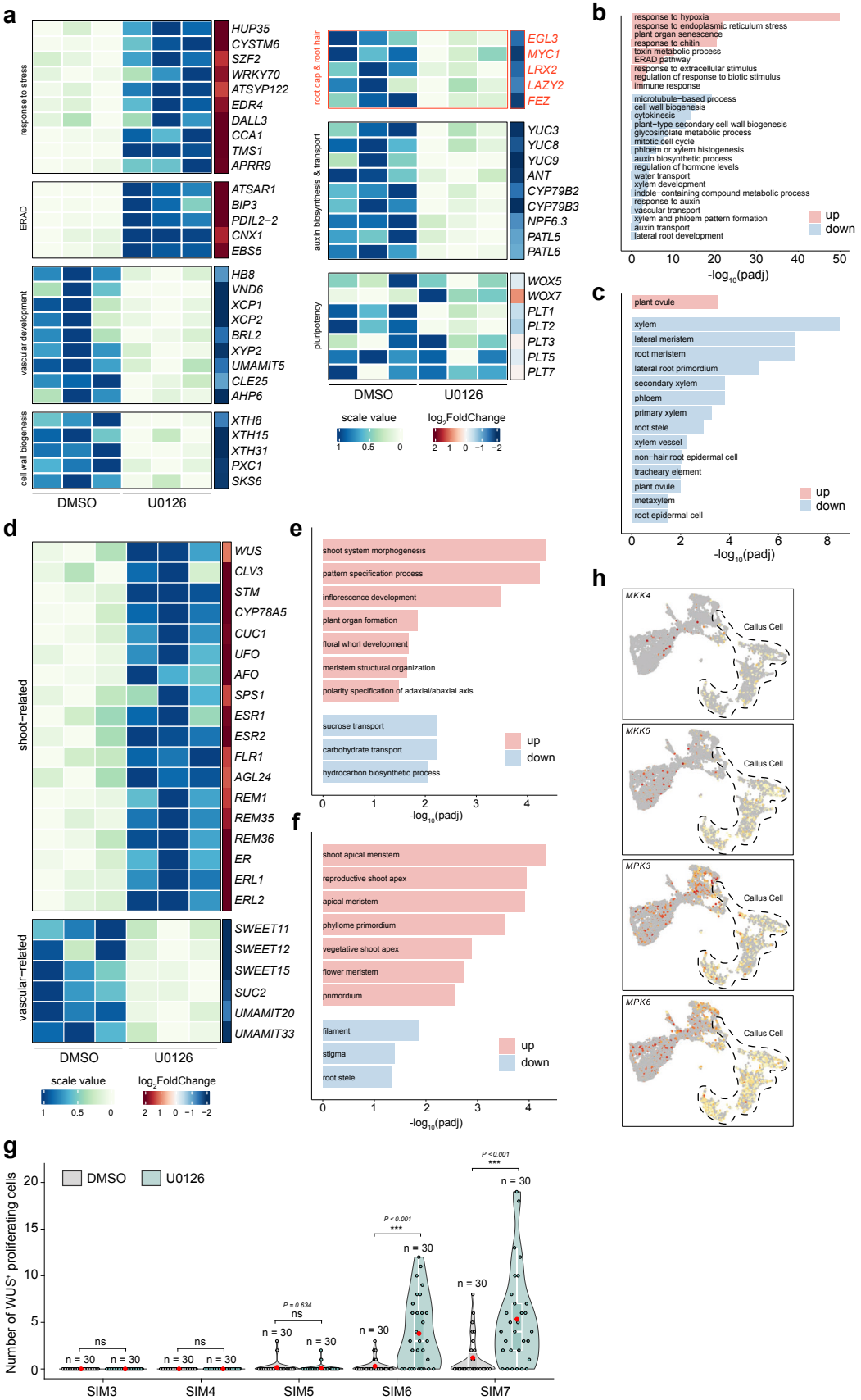
c Quantification of EdU-positive cells per unit area. Statistical analysis was performed using a Student's *t*-test. *** $P < 0.001$; * $P < 0.05$; ns, no significant difference.

d Effects of FVP, HU, and NOCO on callus proliferation and *ACL5* reporter expression. ACL5 reporter explants were cultured on CIM supplemented with 2.5 μM FVP, 5 mM HU, or 5 μM NOCO for 7 days, with DMSO as control. Scale bars, 100 μm.

e, f Quantification of the effects of FVP, HU, and NOCO on the number of $ACL5^{+}$ cells (**e**) and callus area (**f**). Wild-type explants were grown on CIM containing 2.5 μM FVP, 5 mM HU, or 5 μM NOCO, and analyzed at CIM7. Statistical analysis was conducted using one-way ANOVA followed by Tukey's multiple comparisons test. *** $P < 0.001$; * $P < 0.05$; ns, no significant difference.

g Regeneration efficiency following treatment with FVP, HU, or U0126. Wild-type explants were cultured on CIM supplemented with 2.5 μM FVP, 5 mM HU, or 5 μM U0126 for 7 days, then transferred to SIM. The numbers of shoots and roots per explant were quantified at SIM17. Lowercase letters denote statistically significant differences determined by one-way ANOVA with Tukey's multiple comparisons test. It should be noted that NOCO has strong cytotoxicity to plant cells and therefore does not enhance shoot regeneration (data not shown).

h Representative images illustrating the effect of U0126 and U0126-EtOH on the expression pattern of other four outer-layer marker genes. Cell outlines were stained with propidium iodide (magenta). Scale bars, 50 μm.



Supplementary Fig. S14. Supporting data for the molecular mechanism of U0126.

a Heatmap of differentially expressed genes under U0126 treatment. DMSO served as a control. Calli at CIM7 were analyzed. Genes upregulated by U0126 were associated with stress responses and the ERAD pathway, while downregulated genes were linked to vascular development, cell wall synthesis, auxin-related processes, and root cap & root hair development (highlighted in red). Pluripotency-related genes showed mixed expression changes. Scale values reflect expression changes, and $\log_2$FoldChange represents fold change magnitudes. Three biological replicates were included.

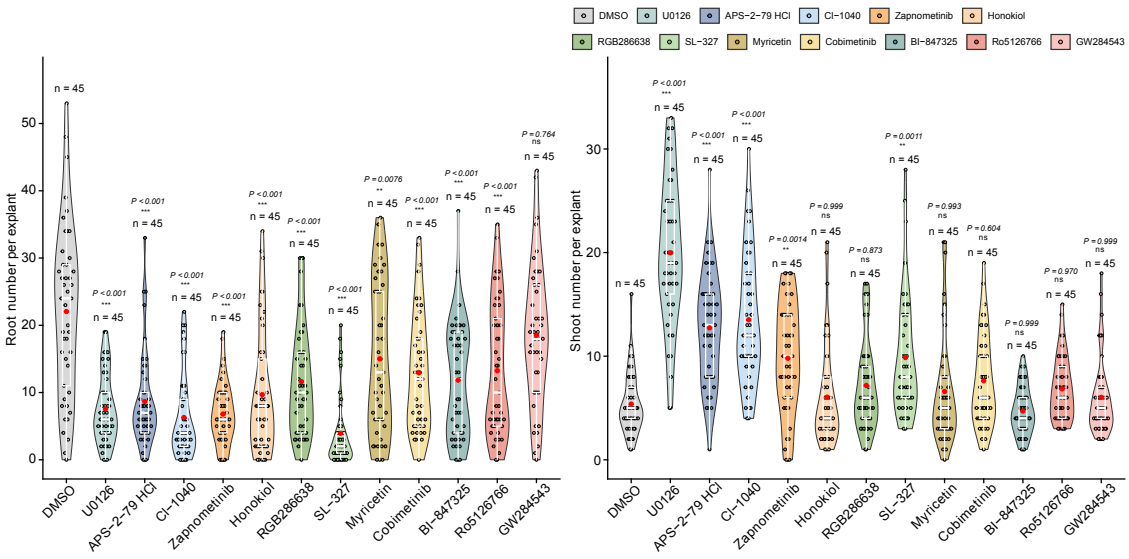
b, c Representative GO (**b**) and PO (**c**) terms enriched among differentially expressed genes under U0126 treatment. Enrichment analysis was based on -$\log_{10}$(padj) values, with thresholds of *padj* < 0.05 and absolute $\log_2$FoldChange > 0.58.

d Heatmap of differentially expressed genes related to shoot (top) and vascular development (bottom) upon U0126 treatment. The wild type (Col-0) explants were cultured on the CIM supplemented with DMSO (control) or 5 μM U0126. The resultant calli at CIM7 were transferred to the SIM. The calli at SIM6 were harvested and subjected to RNA-seq analyses. The changes in expression level are shown by scale values, and the absolute change folds of each gene are shown by $\log_2$FoldChange. Three biological replicates were performed. See also Supplementary Table S1.

e, f Representative GO (**e**) and PO (**f**) terms of differentially expressed genes upon U0126 treatment as described in (**d**). The -$\log_{10}$(padj) values for GO or PO enrichment are given. The threshold for differentially expressed genes used in the GO or PO enrichment analysis was *padj* < 0.05 and an absolute $\log_2$FoldChange greater than 0.58. See also Supplementary Table S1.

g Effects of U0126 on the timing of the appearance of WUS^+ cells on the SIM. We cultured the explants of the *WUS* reporter line (*pWUS::DsRed-N7*) on the CIM supplemented with DMSO (control) or 5 μM U0126. The resultant calli at CIM7 were transferred to the SIM. The number of WUS^+ cells in each callus were counted daily from SIM3 to SIM7. Callus counts are shown at the top of each column. *n* represents the number of callus explants. Statistical analysis was performed using a Student's *t*-test. *** $P < 0.001$; ns, no significant difference.

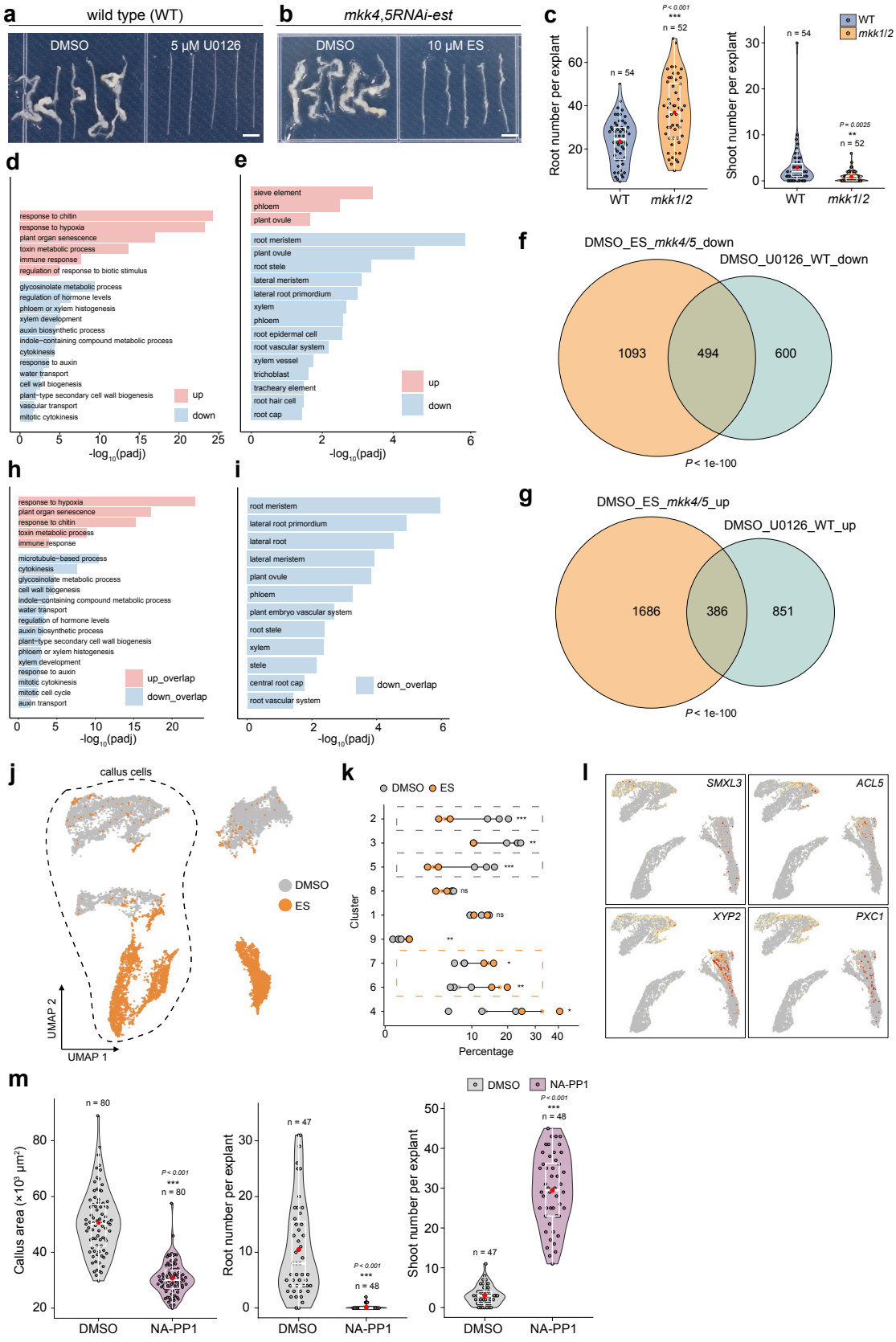
h UMAP plots illustrating the expression patterns of *MKK4*/*5* and *MPK3*/*6* at CIM7. Dashed lines outline callus cells.



Supplementary Fig. S15. Supporting data for the effects of other MEK inhibitors on reducing ineffective callus regions.

We collected 29 compounds targeting MEK. Based on chemical screen as mentioned in the main text, we uncovered 12 compounds including U0126 that could reduce the number of $ACL5^{+}$ cells on the CIM. We then assayed their effects on shoot regeneration. The concentration used was 5 μM. The data are quantified at SIM14 and shown by violin plots. Callus counts are shown at the top of each column. Medians (middle bars), quartiles (boxes), and 1.5× interquartile ranges (whiskers) are indicated. Red dots represent means. *n* represents the number of callus explants. Statistical analysis was performed using one-way ANOVA with Tukey's multiple comparisons. *** $P < 0.001$; ** $P < 0.01$; ns, not significant. Please note that U0126 outperformed other MEK inhibitors.

See also Supplementary Table S1.



Supplementary Fig. S16. Supporting data for U0126 reducing ineffective callus regions through the MKK4/5–MPK3/6 cascade.

a, b Representative images illustrating the effect of U0126 and ES treatment on wild-type (**a**) and *mkk4,5RNAi-est* (**b**) callus development, respectively. Images were taken at CIM21 for wild type and CIM22 for *mkk4,5RNAi-est*. Scale bars, 2 mm.

c Regenerative efficiencies of wild type (Col-0) and the *mkk1/2* mutant. The numbers of regenerated roots (left) and shoots (right) were quantified at SIM16 and displayed as violin plots. Callus counts are shown at the top of each column. Medians (middle bars), quartiles (boxes), and 1.5× interquartile ranges (whiskers) are indicated. Red dots represent means. *n* represents the number of callus explants. Statistical analysis was performed using a Student's *t*-test. *** $P < 0.001$; ** $P < 0.01$.

d, e Representative enriched GO (**d**) and PO (**e**) terms for differentially expressed genes in *mkk4,5RNAi-est* upon ES treatment. Explants were cultured on CIM with DMSO (control) or 10 μM ES. Calli were harvested at CIM7 for RNA-seq. Three biological replicates were included. Enrichment thresholds were *padj* < 0.05 and absolute $\log_2$FoldChange > 0.58.

f, g The intersection of differentially down-regulated (**f**) and up-regulated (**g**) gene sets in ES-treated *mkk4,5RNAi-est* calli and those in U0126-treated wild type (WT) calli. Statistical analysis was performed using hypergeometric distribution tests.

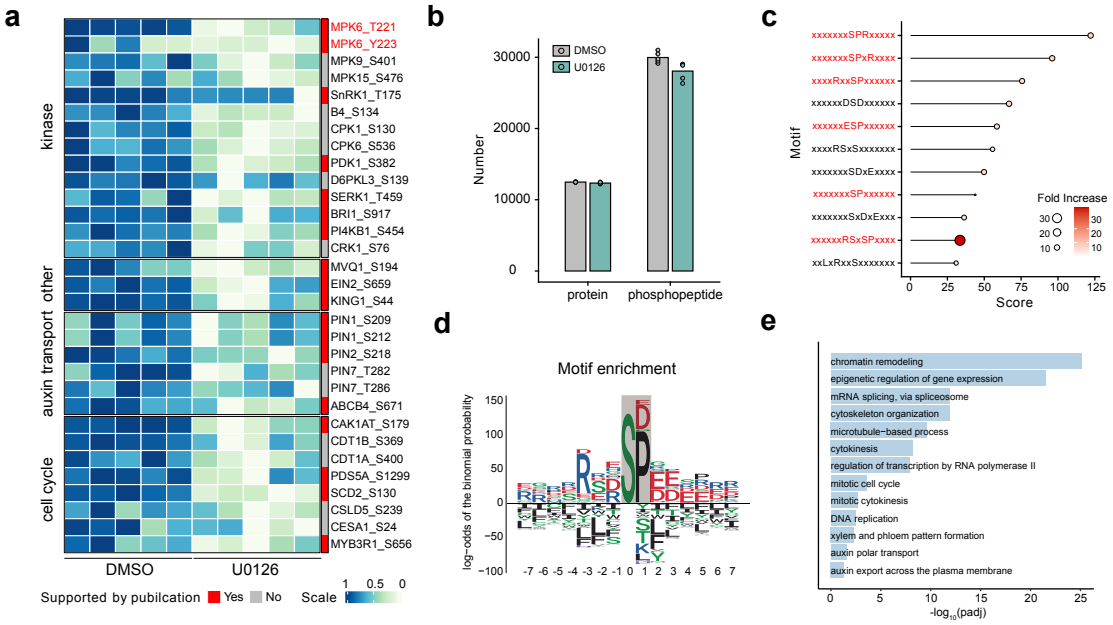
h, i Representative enriched GO (**h**) and PO (**i**) terms for the intersection gene set as described in (**f**, **g**).

j UMAP showing the merged cell atlas of control and ES-treated samples without data integration. The atlas with integration is given in Fig. 6f. Black dashed line indicates the callus cell population. Please note that compared to control sample, the ES-treated calli exhibited weaker cell heterogeneity, an indicative of a high level of callus growth synchronization.

k Changes in cell cluster proportions under ES treatment. Proportions of cell clusters in control (DMSO) and ES-treated samples were quantified. Biological replicates: $n = 3$ for DMSO and $n = 2$ for ES. The x-axis (cluster proportions) was square root transformed for better visualization. Orange and gray boxes indicate clusters with increased or decreased proportions, respectively, under ES treatment. Differential abundance analysis was performed using edgeR. *** $P < 0.001$; ** $P < 0.01$; * $P < 0.05$; ns, not significant.

l UMAPs showing expression patterns of representative genes in clusters 2 and 5, which decreased in proportion under ES treatment.

m Regeneration phenotype of conditional *mpk3*/*6* mutants (*MPK3SR*). Silencing of *MPK3*/*6* was induced by treatment with 0.5 μM NA-PP1 (4-amino-1-tert-butyl-3-(1-naphthyl)pyrazolo[3,4-d]pyrimidine), with DMSO as control [79]. Callus area was measured at CIM7, and root and shoot numbers were quantified at SIM16. Data are presented as violin plots, with callus counts shown above each column. *n* represents the number of callus explants. Medians (center lines), quartiles (boxes), and 1.5× interquartile ranges (whiskers) are indicated. Red dots denote means. Statistical analysis was performed using a Student's *t*-test. *** $P < 0.001$.



Supplementary Fig. S17. Phosphoproteomic analysis of mock- and U0126-treated calli.

a Mass spectrometry-based phosphoproteomic analysis of mock- and U0126-treated calli. Representative phosphopeptides showing reduced phosphorylation in U0126-treated samples are presented, with those supported by published studies indicated. The MPK6 phosphorylation sites (T221 and Y223) targeted by MKK4/5 are highlighted in red. Five biological replicates were analyzed.

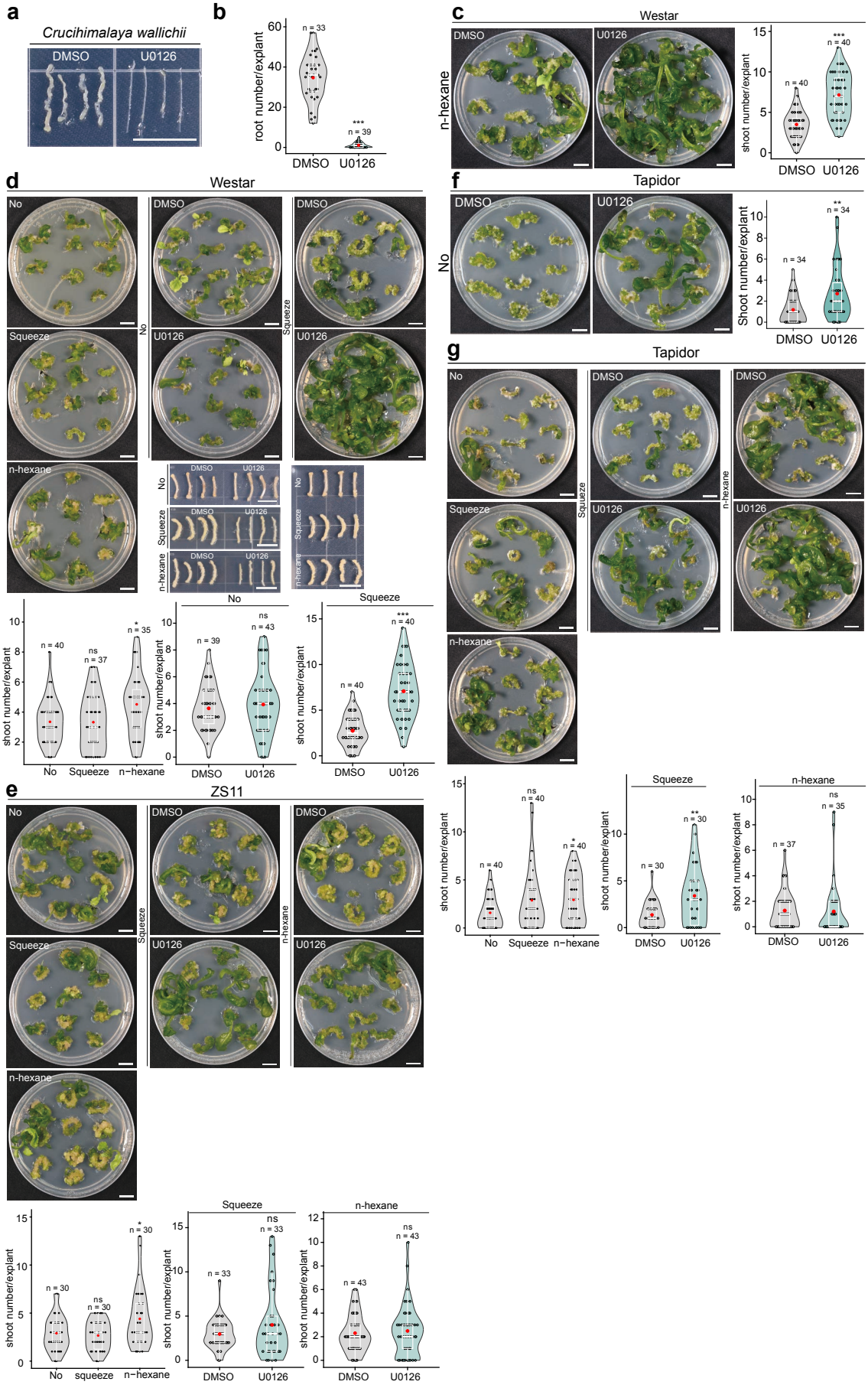
b Numbers of proteins and phosphopeptides identified in mass spectrometry-based phosphoproteomic analysis. Mock (DMSO) and U0126 datasets were combined, with five biological replicates per condition.

c Motif enrichment analysis of downregulated phosphopeptides in U0126-treated samples. The consensus proline-directed SP motif is shown.

d Motif enrichment analysis of downregulated phosphopeptides in U0126-treated samples. The SP motif is highlighted in red.

e Representative enriched GO terms for downregulated phosphopeptides in U0126-treated samples. Thresholds were set at $\log_2$FoldChange < -0.58 and *P*-value < 0.1.

See also Supplementary Table S1.

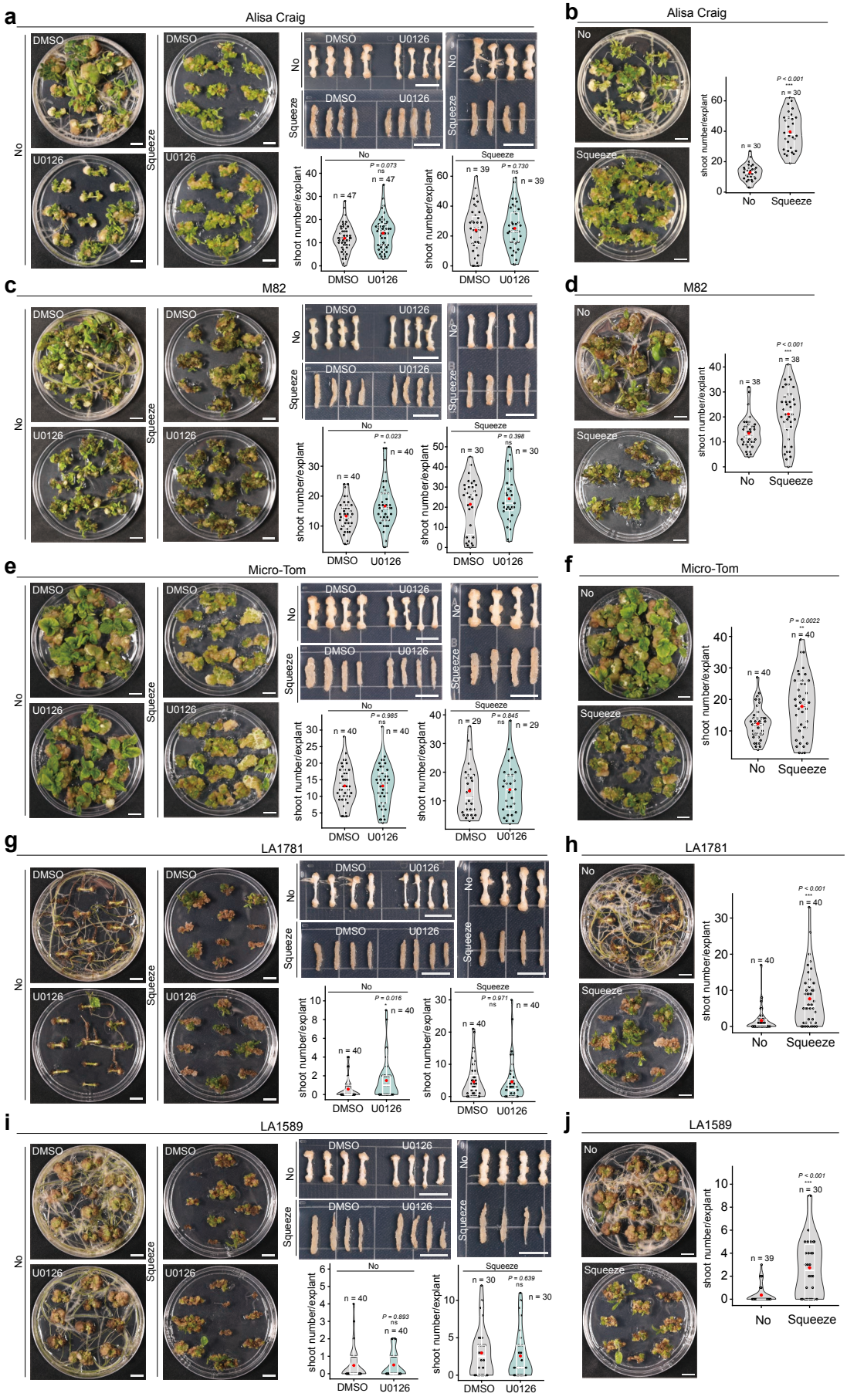

a
Crucihimalaya wallichii
DMSO
U0126
b
root number/explant
n = 33
n = 39
***
DMSO
U0126
c
Westar
n-hexane
DMSO
U0126
shoot number/explant
n = 40
n = 40
***
d
Westar
No
Squeeze
n-hexane
shoot number/explant
n = 40
ns
n = 37
*
n = 35
n = 39
ns
n = 43
n = 40
***
n = 40
No
Squeeze
n−hexane
DMSO
U0126
e
ZS11
No
Squeeze
n-hexane
shoot number/explant
n = 30
ns
n = 30
*
n = 30
n = 33
ns
n = 33
n = 43
ns
n = 43
No
squeeze
n−hexane
DMSO
U0126
f
Tapidor
No
DMSO
U0126
Shoot number/explant
n = 34
**
n = 34
g
Tapidor
No
Squeeze
n-hexane
DMSO
U0126
shoot number/explant
n = 40
ns
n = 40
*
n = 40
n = 30
**
n = 30
n = 37
ns
n = 35
No
Squeeze
n−hexane
DMSO
U0126

Supplementary Fig. S18. Supporting data for the effects of U0126, n-hexane, and squeezing on shoot regeneration efficiency in other Brassicaceae species.

a Representative images illustrating the effect of U0126 on callus development in *C. wallichii*. The images were taken at CIM14. Scale bar, 1 cm.

b Quantitative analyses of the effectiveness of U0126 on root regeneration in *C. wallichii*. Data were quantified at SIM29 and displayed as violin plots. Callus counts are shown at the top of each column. Medians (middle bars), quartiles (boxes), and 1.5× interquartile ranges (whiskers) are indicated. Red dots represent means. Statistical analysis was performed using a Student's *t*-test. *** $P < 0.001$.

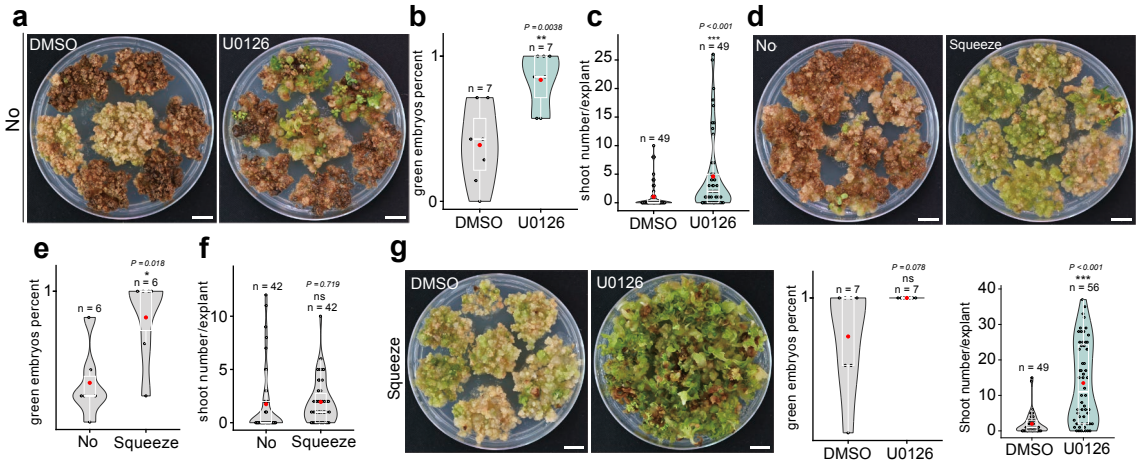
c-g Combined effects of U0126 (**c**, **f**), n-hexane (**d**, **e**, **g**), and squeezing (**d**, **e**, **g**) on shoot regeneration and callus growth in three varieties Westar (**c**, **d**), ZS11 (**e**), and Tapidor (**f**, **g**) of *B. napus*. For quantifications in Westar (**c**, **d**), the data for comparing DMSO and U0126 without additional pretreatment were quantified at SIM19, whereas those for comparing DMSO and U0126 with squeezing pretreatment is at SIM21. For quantifications in ZS11 (**e**), the data for comparing DMSO and U0126 with or without squeezing or n-hexane pretreatment were all quantified at SIM29. For quantifications in Tapidor (**f**, **g**), the data for comparing DMSO and U0126 with or without squeezing or n-hexane pretreatment were all quantified at SIM21. *n* represents the number of callus explants. Representative images for calli at CIM21 are shown. Statistical analysis was performed using one-way ANOVA with Tukey's multiple comparisons. *** $P < 0.001$; ** $P < 0.01$; * $P < 0.05$; ns, not significant. Scale bars, 1 cm.


a
Alisa Craig
DMSO
U0126
No
Squeeze
shoot number/explant
n = 47
n = 39
P = 0.073
P = 0.730
b
Alisa Craig
P < 0.001
n = 30
c
M82
n = 40
n = 30
P = 0.023
P = 0.398
d
M82
n = 38
e
Micro-Tom
n = 29
P = 0.985
P = 0.845
f
Micro-Tom
P = 0.0022
g
LA1781
P = 0.016
P = 0.971
h
LA1781
i
LA1589
P = 0.893
P = 0.639
j
LA1589

Supplementary Fig. S19. Supporting data for the effect of U0126 and squeezing on shoot regeneration efficiency in tomato varieties.

The combined effects of U0126 (**a**, **c**, **e**, **g**, **i**) and squeezing (**b**, **d**, **f**, **h**, **j**) on shoot regeneration and callus growth in three varieties Alisa Craig (**a**, **b**), M82 (**c**, **d**), and Micro-Tom (**e**, **f**) of *S. lycopersicum*, and two varieties LA1781 (**g**, **h**) and LA1589 (**i**, **j**) of *S. pimpinellifolium*. Representative images for calli at CIM14 are shown. For quantifications in Alisa Craig (**a**, **b**), the data for comparing DMSO and U0126 without additional pretreatment were quantified at SIM32, whereas those for comparing DMSO and U0126 with squeezing pretreatment is at SIM33. For quantifications in M82 (**c**, **d**), the data for comparing DMSO and U0126 without additional pretreatment were quantified at SIM28, whereas those for comparing DMSO and U0126 with squeezing pretreatment were also at SIM28. For quantifications in Micro-Tom (**e**, **f**), the data for comparing DMSO and U0126 without additional pretreatment were quantified at SIM32, whereas those for comparing DMSO and U0126 with squeezing pretreatment were at SIM32 as well. For quantifications in LA1781 (**g**, **h**) and LA1589 (**i**, **j**), the data for comparing DMSO and U0126 with or without squeezing pretreatment were quantified at SIM46.

"No" and "squeeze" indicate no additional pre-treatment and squeezing pre-treatments, respectively. The concentration of U0126 used is 50 μM for the samples without pre-treatment and 10 μM for those with squeezing pre-treatments. *n* represents the number of callus explants. Statistical analyses were performed using a Student's *t*-test. *** $P < 0.001$; ** $P < 0.01$; * $P < 0.05$; ns, not significant. Scale bars, 1 cm.



Supplementary Fig. S20. Supporting data showing the effects of U0126 treatment and mechanical squeezing on shoot regeneration efficiency in *Medicago sativa*.

a Representative images showing the effects of U0126 on shoot regeneration in *M. sativa* explants without squeezing. DMSO served as the control.

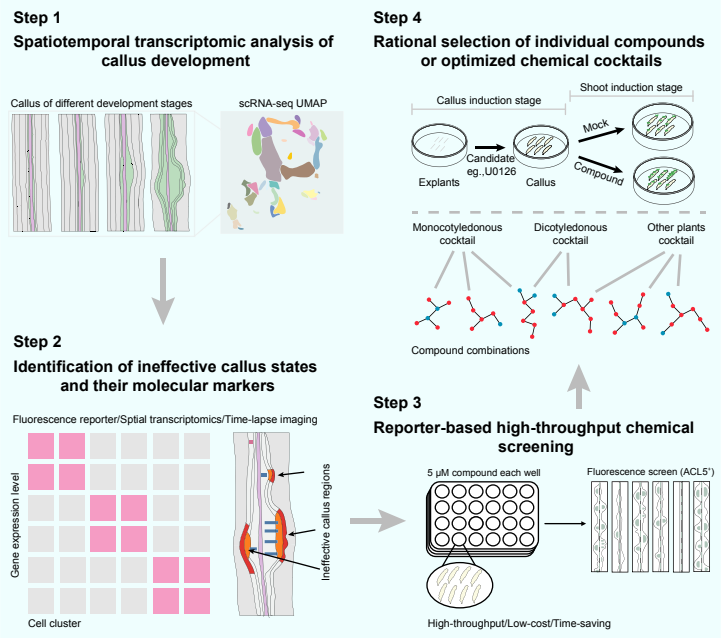
b, c Quantification of U0126 effects on the percentage of green embryos (**b**) and the number of regenerated shoots (**c**). All regeneration assays were conducted without squeezing the explants. *n* represents the number of callus explants.

d Representative images showing the effects of mechanical squeezing on *M. sativa* shoot regeneration.

e, f Quantification of squeezing effects on the percentage of green embryos (**e**) and the number of regenerated shoots (**f**). *n* represents the number of plates.

g Effects of U0126 on the percentage of green embryos under squeezing conditions. The percentage of green embryos represents the proportion of callus in each culture dish exhibiting green spots. *n* represents the number of plates (percentage) or the number of callus explant (shoot number).

Statistical analyses were performed using a Student's *t*-test, *** $P < 0.001$; ** $P < 0.01$; * $P < 0.05$; ns, no significant difference. Scale bars in (**a**, **d**), 1 cm.



Supplementary Fig. S21. A four-step framework for optimizing regeneration.

Our results establish a four-step framework for regeneration optimization. First, spatiotemporal transcriptomic profiling of callus development in the target species reveals cellular heterogeneity and distinct cell populations. Second, live or time-lapse imaging is integrated with molecular analyses to identify ineffective callus regions and their defining markers. Third, these markers are used to construct reporter systems for chemical screening; when combined with a 24-well plate–based liquid culture platform, this approach increases throughput while reducing time and compound costs. Finally, candidate compounds are validated based on shoot regeneration efficiency. Notably, regeneration failure reflects not only species-specific genotypes and developmental programs but also defects at the SIM stage, rendering a single universal compound unlikely. Future efforts that optimize existing compounds and identify species- or family-specific compounds or cocktails acting at distinct regeneration stages should ultimately overcome major constraints in plant regeneration.

Supplementary References

1 Wu, L. Y. *et al.* Dynamic chromatin state profiling reveals regulatory roles of auxin and cytokinin in shoot regeneration. *Dev Cell* **57**, 526-542, doi:10.1016/j.devcel.2021.12.019 (2022).

2 Takada, S., Takada, N. & Yoshida, A. ATML1 promotes epidermal cell differentiation in Arabidopsis shoots. *Development* **140**, 1919-1923, doi:10.1242/dev.094417 (2013).

3 Zhou, Y. P., Duan, J., Fujibe, T., Yamamoto, K. T. & Tian, C. E. AtIQM1, a novel calmodulin-binding protein, is involved in stomatal movement in Arabidopsis. *Plant Mol Biol* **79**, 333-346, doi:10.1007/s11103-012-9915-0 (2012).

4 Ohashi-Ito, K. *et al.* A bHLH complex activates vascular cell division via cytokinin action in root apical meristem. *Curr Biol* **24**, 2053-2058, doi:10.1016/j.cub.2014.07.050 (2014).

5 De Rybel, B. *et al.* A bHLH complex controls embryonic vascular tissue establishment and indeterminate growth in Arabidopsis. *Dev Cell* **24**, 426-437, doi:10.1016/j.devcel.2012.12.013 (2013).

6 Zhang, T. Q., Chen, Y. & Wang, J. W. A single-cell analysis of the Arabidopsis vegetative shoot apex. *Dev Cell* **56**, 1056-1074., doi:10.1016/j.devcel.2021.02.021 (2021).

7 Iwase, A. *et al.* The AP2/ERF transcription factor WIND1 controls cell dedifferentiation in Arabidopsis. *Curr Biol* **21**, 508-514 (2011).

8 Ikeuchi, M., Rymen, B. & Sugimoto, K. How do plants transduce wound signals to induce tissue repair and organ regeneration? *Curr Opin Plant Biol* **57**, 72-77, doi:10.1016/j.pbi.2020.06.007 (2020).

9 Iwase, A. *et al.* WIND transcription factors orchestrate wound-induced callus formation, vascular reconnection and defense response in Arabidopsis. *New Phytol* **232**, 734-752, doi:10.1111/nph.17594 (2021).

10 Iwase, A. *et al.* WIND1 Promotes Shoot Regeneration through Transcriptional Activation of ENHANCER OF SHOOT REGENERATION1 in Arabidopsis. *Plant Cell* **29**, 54-69, doi:10.1105/tpc.16.00623 (2017).

11 Zhai, N. & Xu, L. Pluripotency acquisition in the middle cell layer of callus is required for organ regeneration. *Nat Plants* **7**, 1453-1460, doi:10.1038/s41477-021-01015-8 (2021).

12 Sugimoto, K., Jiao, Y. & Meyerowitz, E. M. Arabidopsis regeneration from multiple tissues occurs via a root development pathway. *Dev Cell* **18**, 463-471 (2010).

13 Ogura, N. *et al.* WUSCHEL-RELATED HOMEOBOX 13 suppresses de novo shoot regeneration via cell fate control of pluripotent callus. *Sci Adv* **9**, eadg6983, doi:10.1126/sciadv.adg6983 (2023).

14 Eshed Williams, L. Genetics of Shoot Meristem and Shoot Regeneration. *Annu Rev Genet* **55**, 661-681, doi:10.1146/annurev-genet-071719-020439 (2021).

15 He, C., Chen, X., Huang, H. & Xu, L. Reprogramming of H3K27me3 is critical for acquisition of pluripotency from cultured Arabidopsis tissues. *PLoS Genet* **8**, e1002911, doi:10.1371/journal.pgen.1002911 (2012).

16 Kaya-Okur, H. S. *et al.* CUT&Tag for efficient epigenomic profiling of small samples and single cells. *Nat Commun* **10**, 1930, doi:10.1038/s41467-019-09982-5 (2019).

17 Buenrostro, J. D., Giresi, P. G., Zaba, L. C., Chang, H. Y. & Greenleaf, W. J. Transposition of native chromatin for fast and sensitive epigenomic profiling of open chromatin, DNA-binding proteins and nucleosome position. *Nat Methods* **10**, 1213-1218, doi:10.1038/nmeth.2688 (2013).

18 Wang, F. X. *et al.* Protocol for assaying chromatin accessibility using ATAC-seq in plants. *STAR Protoc* **2**, 100289, doi:10.1016/j.xpro.2020.100289 (2021).

19 Crispatzu, G. *et al.* The chromatin, topological and regulatory properties of pluripotency-associated poised enhancers are conserved *in vivo*. *Nat Commun* **12**, 4344, doi:10.1038/s41467-021-24641-4 (2021).

20 Zhao, C. *et al.* MAP Kinase Cascades Regulate the Cold Response by Modulating ICE1 Protein Stability. *Dev Cell* **43**, 618-629 e615, doi:10.1016/j.devcel.2017.09.024 (2017).

21 Kuhn, A. *et al.* RAF-like protein kinases mediate a deeply conserved, rapid auxin response. *Cell* **187**, 130-148 e117, doi:10.1016/j.cell.2023.11.021 (2024).

22 Songyang, Z. *et al.* A structural basis for substrate specificities of protein Ser/Thr kinases: primary sequence preference of casein kinases I and II, NIMA, phosphorylase kinase, calmodulin-dependent kinase II, CDK5, and Erk1. *Mol Cell Biol* **16**, 6486-6493, doi:10.1128/MCB.16.11.6486 (1996).

23 Lewis, T. S., Shapiro, P. S. & Ahn, N. G. Signal transduction through MAP kinase cascades. *Adv Cancer Res* **74**, 49-139, doi:10.1016/s0065-230x(08)60765-4 (1998).

24 Pitzschke, A. Modes of MAPK substrate recognition and control. *Trends Plant Sci* **20**, 49-55, doi:10.1016/j.tplants.2014.09.006 (2015).

25 Hao, N. *et al.* Novel lignin-based extracellular barrier in glandular trichome. *Nat Plants* **10**, 381-389, doi:10.1038/s41477-024-01626-x (2024).

26 Wendrich, J. R. *et al.* Vascular transcription factors guide plant epidermal responses to limiting phosphate conditions. *Science* **370**, eaay4970, doi:10.1126/science.aay4970 (2020).

27 Cheng, Y. J. *et al.* Cell division in the shoot apical meristem is a trigger for miR156 decline and vegetative phase transition in Arabidopsis. *Proc Natl Acad Sci U S A* **118**, e2115667118, doi:10.1073/pnas.2115667118 (2021).

28 Yin, K. *et al.* A dual-color marker system for in vivo visualization of cell cycle progression in Arabidopsis. *Plant J* **80**, 541-552, doi:10.1111/tpj.12652 (2014).

29 Desvoyes, B., Arana-Echarri, A., Barea, M. D. & Gutierrez, C. A comprehensive fluorescent sensor for spatiotemporal cell cycle analysis in Arabidopsis. *Nat Plants* **6**, 1330-1334, doi:10.1038/s41477-020-00770-4 (2020).